



Dynamics of Phase Transitions and Hysteresis in a Viscoelastic Ericksen's Bar on an Elastic Foundation

ANNA VAINCHTEIN

Division of Mechanics and Computation, Department of Mechanical Engineering, Stanford University, Stanford, CA 94305, U.S.A. E-mail: annav@leland.stanford.edu
Current address: Department of Mathematics, 301 Thackeray Hall, University of Pittsburgh, Pittsburgh, PA 15260, U.S.A. E-mail: annav@math.pitt.edu

Received 23 November 1999; in revised form 6 June 2000

Abstract. This work is a follow-up on the study [32] of interface dynamics and hysteresis in materials undergoing solid-solid phase transitions. We consider the dynamics of a viscoelastic bar with a nonmonotone stress-strain relation and viscous stress linearly proportional to the strain rate. The bar is placed on an elastic foundation with stiffness β mimicking the interaction of phases in higher dimensions. Time-dependent displacement-controlled loading of the bar results in a tilted and serrated hysteresis loop, in qualitative agreement with some experimental observations in shape-memory alloys. The model exhibits three phase transition processes: phase nucleation, interface slip and phase annihilation. Between these dynamic processes the system gets stuck in local minimizers of the potential energy. As β increases from zero, a slip-dominated solution behavior transforms to the one where slip and annihilation events are preceded by a step-by-step nucleation process. We show that this transition is caused by an interplay between the slip-favoring inertia term and the nucleation-favoring elastic foundation terms.

Key words: dynamics, phase transformation, hysteresis, microstructures, viscoelastic material.

1. Introduction

Materials undergoing stress-induced martensitic phase transitions often form a variety of finely layered microstructures and exhibit hysteretic behavior when subjected to cyclic loading [6, 9, 16, 17, 19, 24, 25].

Following the pioneering work of Ericksen [7], who has studied equilibria of an elastic bar with a nonmonotone stress-strain curve, it has become common to describe these phenomena by employing a nonconvex elastic energy density [1, 2, 4, 5, 12, 22, 23]. Material phases are represented by the potential wells in the energy density function. The absolute minimization of such potential energy captures basic features of the microstructure [14] but cannot explain hysteresis, which arises when the material gets locked in metastable states [8, 18]. Other studies of hysteresis in shape-memory alloys include [1, 3, 5, 15, 22].

This work is partially motivated by the studies in [4, 10, 11] of the dynamics of a viscoelastic Ericksen's bar with a nonconvex elastic energy density. The bar is placed on an elastic foundation and subjected to zero displacement boundary conditions. The viscous stress is linearly proportional to the strain rate. The statics analysis shows that the elastic foundation makes finer and finer phase mixtures energetically more favorable. The limit of energy-minimizing sequences can be described by a Young-measure solution (generalized limit of rapidly oscillating function sequences). However, the numerical results in [4] show that the dynamic solutions typically tend to the states with finitely many interfaces. These states locally minimize the potential energy with respect to smooth perturbations that leave the phase boundaries frozen. Following [28], we will refer to these states as *elastic minimizers*. The dynamic stability of these minimizers was confirmed analytically in [10, 11]. The finite scale of phase layering also agrees with experimental results [24, 25].

Zero-displacement boundary conditions used in [4] force the energy to decrease with time and thus facilitate the analysis of the asymptotic behavior of solutions. However, in order to obtain a nontrivial solution, one has to pick various nonzero initial conditions in this case. These conditions often correspond to unstable states, and their physical meaning is unclear. Moreover, the large-time solution behavior is very sensitive to the choice of initial conditions. In particular, one can find a sequence of Young-measure initial states each of which generates a solution that tends to an absolute energy minimizer in the large-time limit [27]. But does a material get in these initial states?

Motivated by a desire to model experiments such as the tension test, the paper [32] considered a special case of this model, without the elastic foundation, with *time-dependent* boundary conditions. In this work a physically appropriate stress-free stable state was chosen as an initial condition, and control of the loading rate was allowed. This facilitated a study of the overall hysteretic behavior during a loading-unloading cycle. As demonstrated in [7], in this case there are infinitely many elastic equilibria. Each elastic equilibrium has a piecewise constant, discontinuous strain. The strain discontinuities can be thought of as phase boundaries. These sharp interfaces cannot move [20]. It has been shown in [32] that with sufficiently slow loading, the dynamic solution that started in a stress-free single-phase state follows closely a branch of metastable single-phase equilibria that emerge from the initial state, until the time-dependent loading causes the strain to enter the *spinodal region*, or the region where the elastic energy density is concave. The spinodal instability then results in *phase nucleation*, with several sharp phase boundaries. We note that nucleation process described here occurs via *spinodal decomposition* since it happens after a portion of the bar has strain in the spinodal region and does not involve overcoming an energy barrier typical of the systems jumping from one local energy minimum to another. After nucleation, the solution undergoes two different regimes. In the *stick* regime, it gets stuck in one of the quasistatic branches consisting of elastic equilibria with fixed positions of the

phase boundaries. While the interfaces do not move, the strain in the bar grows in order to adjust to the loading. The solution stays on the branch until the strain enters the spinodal region in part of the bar. In what is called a *slip* regime, the spinodal instability smoothens the strain profile and moves the interfaces to their new locations. This results in *serrations*, or “teeth”, on the overall load-elongation curve. The results in [29] suggest that the stick-slip interface motion is a singular limit of the dynamic model with interfacial energy modeled by a strain-gradient term as the strain-gradient coefficient tends to zero. Both serrations and the stick-slip interface motion have been experimentally observed in shape-memory alloys [9, 16, 17, 19]. The overall shape of the loop is in qualitative agreement with these experimental results. The hysteresis persists even at a very slow loading when viscosity effects are small.

The present paper extends the work [32] by considering the viscoelastic Ericksen’s bar placed on an elastic foundation. The extension is motivated by the fact that most phase-transition phenomena are at least two-dimensional and may not be captured by a simple one-dimensional model. Introducing an elastic foundation into the model allows one to capture some of the higher-dimensional features within a relatively tractable one-dimensional model. The foundation term mimics the interaction of phases in higher dimensions where the displacement field is much more severely constrained by the boundary conditions than in the one-dimensional case. Rewritten in terms of strains, it becomes a nonlocal integral term with a negative-definite interaction kernel; such kernels favor oscillations in strain [21]. The nonlocality is similar to a magnetic field in magnetics. It introduces a length scale of the bar thickness into the model.

Our work also extends the model studied in [4] to the case of *time-dependent* boundary conditions. This allows us to simulate the tension experiments and study the overall hysteresis loops.

The foundation is relaxed at the strain $u' = d_*$ that gives the maximal energy density in the spinodal region (in our simulations we choose elastic energy density with $d_* = 0$ but this choice is not essential and similar results can be obtained without it). As one expects from the results mentioned above, in this case the system also gets locked in the branches of elastic equilibria. We show that there is an interesting interplay between phase nucleation, stick-slip interface motion and *phase annihilation* (coalescence of a pair of interfaces) as three different processes of phase transitions. When the elastic foundation stiffness β is large enough for the given loading (or the loading is sufficiently slow at a given β) the following solution behavior is observed as the bar is loaded from its initial single-phase equilibrium state. At the end displacement d below d_* , only phase nucleation takes place, with new phase boundaries emerging while the old ones are frozen. The stick-slip interface motion and phase annihilation become possible only when d exceeds d_* . This result is not obvious because a dynamic solution may get locked in *any* branch of metastable equilibria that has less energy than the current unstable state, and it is not clear a priori why it prefers to nucleate new boundaries instead of

moving the existing ones at d below d_* . We show that this preference is determined to a large extent by the strain nonuniformities in elastic equilibria.

The hysteresis loop is now tilted and exhibits a large number of serrations in qualitative agreement with some experiments [9, 19]. When $d \leq d_*$ during loading, a finely layered microstructure is formed in a step-by-step nucleation process. The elastic foundation promotes a formation of a large but finite number of boundaries. This number increases as the loading rate gets smaller. At some d above d_* , the boundaries start to move toward each other in a stick-slip fashion, with a pair of boundaries moving from the ends of the bar while other interfaces are frozen. When two boundaries are close enough, phase annihilation takes place.

In contrast, when β is zero or small, the phase boundaries, once formed, start moving via a succession of slip events, even at d below d_* , and most serrations are caused by the slip and annihilation events.

Using a linearized dynamics approach, we show that there are three terms governing the evolution of instabilities. The first term is the inertia force due to loading. The other two terms are due to the strain nonuniformities in elastic equilibria and the bonding force caused by the deformation of springs in the elastic foundation, respectively. In the no-foundation case, only the inertia-force term is present. It favors the stick-slip interface motion even at d below d_* [32]. The terms due to elastic foundation prefer phase nucleation when d does not exceed d_* , but slip and annihilation may occur otherwise. When β is large enough, or the inertia force is small, these terms dominate, and solution behavior just described takes place. At small β , the dynamics is dominated by the inertia force, and the interface slip may occur even at d below d_* .

Our work suggests that nucleation is at least as important cause of the end-load serrations as the interface motion. It also emphasizes the role of strain nonuniformities in the phase intervals in elastic equilibria, occurring in higher-dimensions due to the incompatibility with the boundary conditions and captured here by the elastic foundation term. Depending on the boundary conditions, these nonuniformities, upon entering the spinodal region, may cause nucleation, slip or annihilation process. The work also highlights phase annihilation as another important process causing serrations that has not received attention in the previous work.

The structure of the paper is as follows. We formulate the problem in Section 2. The equilibria are described in Section 3. The main numerical results are described in Section 4. The structure of elastic minimizers is described in Section 5. Linearized dynamics is discussed in Section 6. Finally, Section 7 contains concluding remarks.

2. Problem Formulation

Consider a viscoelastic bar of unit initial length. Let $x \in [0, 1]$ and $u(x, t)$ be the reference coordinate and the longitudinal displacement field, respectively. The elastic strain energy density of the bar is given by $W(u_x)$, where u_x is the defor-

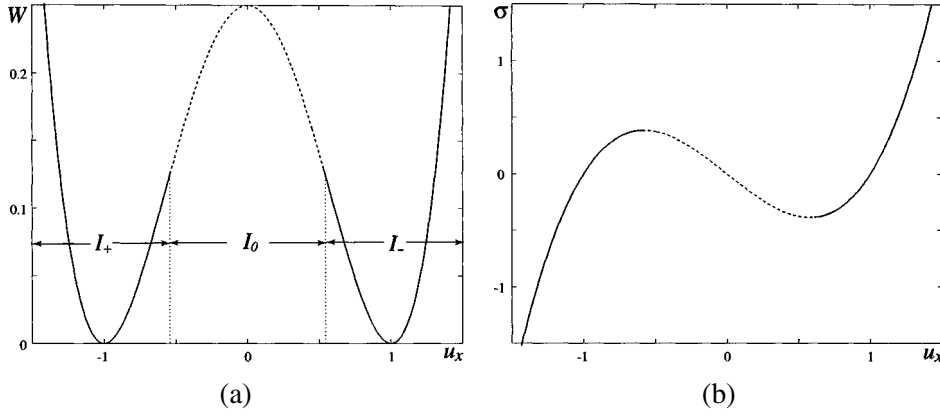


Figure 1. (a) Energy density $W(u_x)$ and (b) stress $\sigma(u_x) \equiv W'(u_x)$.

mation strain. Following the idea introduced in [7], we assume that $W(u_x)$ has two wells connected by a nonconvex region. Each well represents a material phase. For example, one may consider the function

$$W(u_x) = \frac{1}{4}(u_x^2 - 1)^2 \quad (1)$$

which is convex in the intervals $I_+ = (-\infty, -1/\sqrt{3})$, $I_- = (1/\sqrt{3}, \infty)$ and nonconvex when strain is in the interval $I_0 = [-1/\sqrt{3}, 1/\sqrt{3}]$. See Figure 1. We will refer to the intervals I_+ and I_- as + and - *phase intervals*, respectively. The interval of nonconvexity I_0 is called the *spinodal region*. The bar is placed on an elastic foundation (a continuous system of linear noninteracting springs) with stiffness β . The total potential energy of the system is given by

$$E_{\text{pot}} = \int_0^1 [W(u_x) + \beta u^2] dx. \quad (2)$$

Let ρ be the density of the bar in the reference configuration. Assume that the viscous stress is linearly proportional to the strain rate u_{xt} , so that the total stress in the bar is given by $\Sigma = \sigma(u_x) + \gamma u_{xt}$, where $\sigma(u_x) \equiv W'(u_x)$ and γ is a positive constant. The bar is subject to *time-dependent* displacement-controlled boundary conditions. The dynamics of the bar is then described by the following initial-boundary-value problem:

$$\begin{cases} \rho u_{tt} = [\sigma(u_x) + \gamma u_{xt}]_x - 2\beta u, \\ u(0, t) = -\frac{d(t)}{2}, \\ u(1, t) = \frac{d(t)}{2}, \\ u(x, 0) = u_0(x), \\ u_t(x, 0) = 0. \end{cases} \quad (3)$$

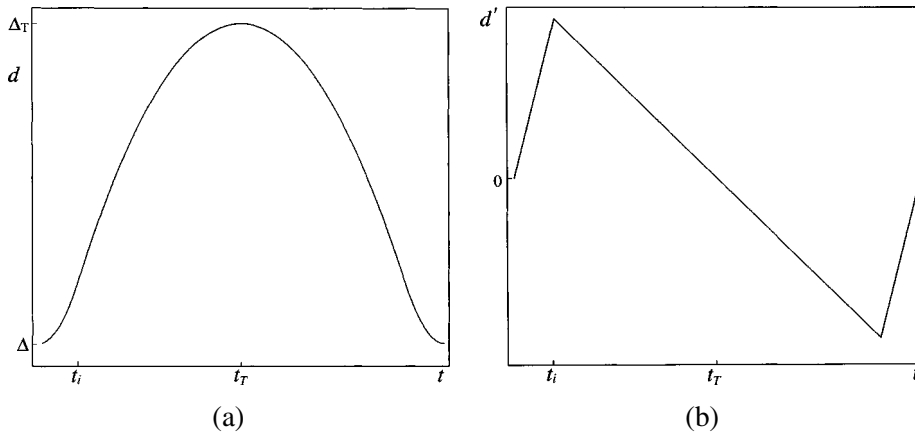


Figure 2. (a) Cyclic loading function $d(t)$ and (b) loading rate $d'(t)$ used in numerical simulations.

Here $d(t)$ is the loading function. In our numerical examples we will employ the following cyclic loading function:

$$d(t) = \begin{cases} (\Delta_T - \Delta) \frac{t^2}{t_i t_T} + \Delta & \text{for } 0 \leq t \leq t_i, \\ (\Delta_T - \Delta) \left[-\frac{(t - t_i)^2}{t_T(t_T - t_i)} + 2\frac{t}{t_T} - \frac{t_i}{t_T} \right] + \Delta & \text{for } t_i \leq t \leq 2t_T - t_i, \\ (\Delta_T - \Delta) \frac{(t - 2t_T)^2}{t_i t_T} + \Delta & \text{for } 2t_T - t_i \leq t \leq 2t_T. \end{cases} \quad (4)$$

Here Δ , Δ_T , t_i , t_T are constants. Graphs of the loading function $d(t)$ and the loading rate $d'(t)$ are shown in Figure 2. The initial end displacement is $d(0) = \Delta$. Loading occurs with d increasing up to a maximum $d(t_T) = \Delta_T$ at $t = t_T$, followed by unloading to the initial value $d(2t_T) = \Delta$. The parameter t_T is inversely proportional to the loading rate amplitude. Parameter t_i controls the initial acceleration $d''(0)$. The initial condition $u_0(x)$ is a stable equilibrium in a + phase at $d = d(0)$, and the initial velocity is zero.

One can show that the rate of change of total (potential plus kinetic) energy is equal to

$$E'(t) = S(t)d'(t) - \gamma \int_0^1 u_{xt}^2 dx. \quad (5)$$

Here $S(t)$ is the end load given by

$$S(t) = \frac{1}{2} [\Sigma(0, t) + \Sigma(1, t)]. \quad (6)$$

The term $S(t)d'(t)$ in (5) is the *loading power*; it supplies energy into the system. The second term, $\gamma \int_0^1 u_{xt}^2 dx$, in (5) is the *energy dissipation rate* caused by the presence of viscous stresses.

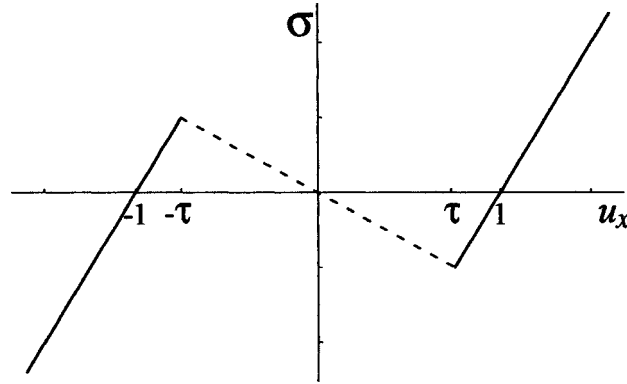


Figure 3. Stress $\sigma(u_x)$ for a trilinear material (7).

In the following sections we will sometimes use a so-called *trilinear* material employed, e.g., in [2], with the stress-strain law given by

$$\sigma(u_x) = \begin{cases} \sigma_+(u_x) = 2(u_x + 1) & \text{for } u_x \leq -\tau, \\ \sigma_0(u_x) = -\theta u_x & \text{for } -\tau < u_x < \tau, \\ \sigma_-(u_x) = 2(u_x - 1) & \text{for } u_x \geq \tau. \end{cases} \quad (7)$$

Here $-\theta = 2(\tau - 1)/\tau < 0$ is the negative slope of the stress-strain curve in the spinodal range. See Figure 3. In effect this replaces W in (1) by a piecewise quadratic function, concave in the spinodal region $|u_x| \leq \tau$, but convex elsewhere (phases).

3. Equilibria

In this section we describe the equilibrium solutions of (3). As in [7], assume that the displacement field $u(x)$ is continuous but the strain u_x may be a piecewise continuous function of x , with N finite jumps at $x = c_i$, $i = 1, \dots, N$. Then in each interval (c_i, c_{i+1}) the equilibria satisfy the following equation:

$$W(u_x) - u_x \sigma(u_x) + \beta u^2 = \text{const} \quad (8)$$

which is the first integral of (3)₁ in the statics case. The boundary conditions are

$$u(0) = -\frac{d}{2}, \quad u(1) = \frac{d}{2}. \quad (9)$$

Equilibria have either smooth (one-phase equilibria) or piecewise continuous strain (multiphase equilibria). In the latter case, the jump locations c_i , are the phase boundaries.

Following the notation introduced in [28], we will consider two classes of multiphase equilibria. The *elastic* equilibria satisfy (8), (9) and the jump conditions

$$[[\sigma(u_x)]]_{c_i} = 0 \quad (10)$$

across the strain discontinuities $x = c_i$. Condition (10) ensures the stress continuity. Such solutions extremize the potential energy functional (2) with respect to $W^{1,\infty}$ variations (with the norm $\|u\|_{1,\infty} = \|u\|_\infty + \|u_x\|_\infty$, $\|u\|_\infty = \text{ess sup}_{x \in [0,1]} |u(x)|$) that leave the locations of jumps c_i frozen. If we allow continuous variations in c_i as well, an additional Weierstrass–Erdman corner condition [13] has to be satisfied:

$$\llbracket W(u_x) - u_x \sigma(u_x) \rrbracket_{c_i} = 0 \quad (11)$$

at each interface. Solutions that satisfy (8)–(11) are called *phase equilibria*. Clearly, a phase equilibrium is an elastic equilibrium. By definition, these equilibria extremize the energy of elastic equilibria as a function of c_i , $i = 1, \dots, N$, at given N and d . Conditions (10) and (11) together imply that the strain in phase equilibria jumps between the so-called *Maxwell strains* e_1 and e_2 which share a common tangent to $W(u_x)$. In case of (1) these are $e_{1,2} = \mp 1$. Note that in elastic equilibria strain can jump between any two strains that give the same value of stress.

If the condition

$$W''(u_x) > 0 \quad (12)$$

is satisfied, elastic equilibria are local energy minimizers with respect to $W^{1,\infty}$ perturbations (both variations and their derivatives are small). Such local minimizers are called *weak* [13]. In contrast, *strong* local energy minimizers are the states that minimize energy with respect to L^∞ variations (with the norm $\|u\|_\infty$ defined above; only variations are small but their derivatives need not be) of the displacement field. A strong local energy minimizer is a phase minimizer, but the converse is not true in general since phase equilibria extremize energy in a weaker ($W^{1,\infty}$) topology. Finally, a strong local minimizer that has the least energy at given d is an *absolute* minimizer in L^∞ topology.

Case $\beta = 0$. This problem was considered in [7]. In this case the equilibrium equation reduces to

$$\sigma(u_x) = \text{const} \quad (13)$$

which is satisfied for all x in $(0, 1)$. Elastic equilibria have piecewise constant strain which alternates between the values w_+ and w_- such that $\sigma(w_+) = \sigma(w_-) = S$ and

$$w_+ \lambda_+ + w_-(1 - \lambda_+) = d. \quad (14)$$

Here λ_+ is the total length of the portion of the bar that has strain w_+ . Condition (14) ensures that the boundary conditions (9) are satisfied. Elastic minimizers are shown on a load-displacement diagram in Figure 4(a). To facilitate the comparison with nonzero- β case, where this choice simplifies the calculations, we show here the minimizers for a trilinear material (7). See, however, [32] for the case of fully

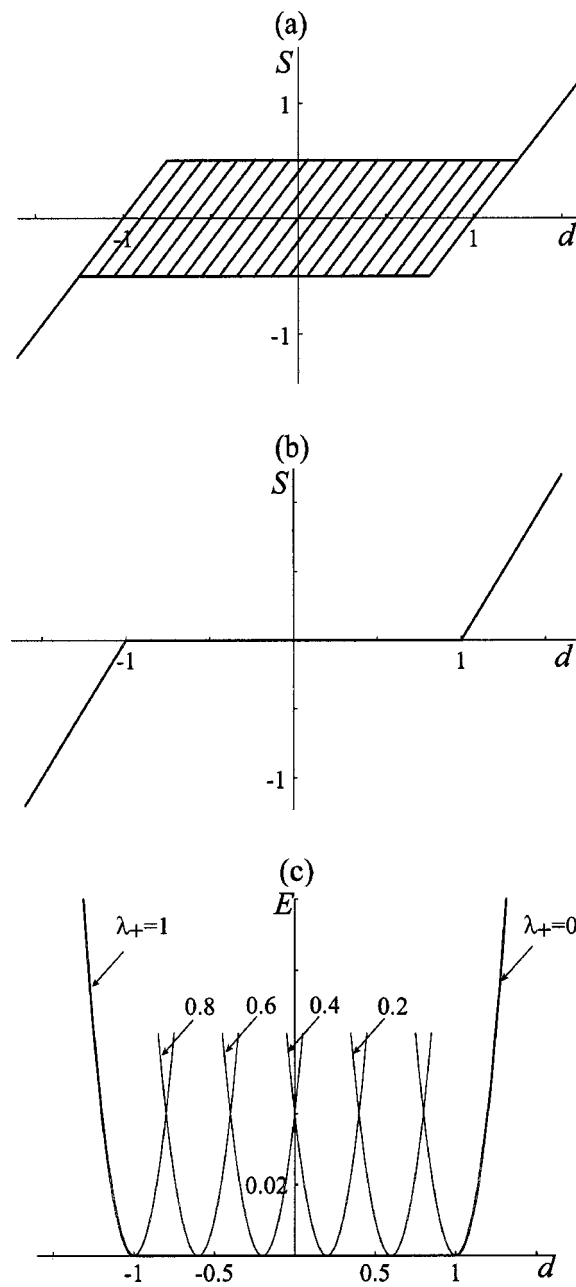


Figure 4. Stable equilibria for the trilinear material (7) with $\tau = 0.75$ in $\beta = 0$ case. (a) Load-displacement diagram of elastic minimizers. Every point inside and on the loop is an elastic minimizer. Tilted parallel lines show branches of equilibria with fixed locations of phase boundaries. The volume fraction of the + phase decreases from left to right. (b) Load-displacement diagram of absolute energy minimizers. (c) Energy of absolute minimizers (thick curves) and several branches of elastic minimizers (thin curves) with different volume fractions λ_+ of the + phase.

nonlinear material (1). There is an *uncountable infinity* of elastic minimizers, and every point inside and on the loop shown in Figure 4(a) represents an elastic minimizer. Each of the parallel straight lines shown (and any line parallel to these) is a branch of elastic minimizers with frozen locations of the interfaces, and therefore, fixed volume fraction λ_+ of the + phase. In case of a fully nonlinear material (1) the straight lines are replaced by curves with inflection points at the ends [32].

In phase equilibria the strain alternates between the Maxwell strains (minimum strains in + and – phase), and any arrangement of phases satisfying (14) gives zero potential energy. Thus phase equilibria are absolute energy minimizers in this case. See Figures 4(b), (c). Observe that the number of interfaces in equilibria is arbitrary in this case since the relation (14) and the equilibrium equation (13) only determine the *volume fractions* of each phase for a given d .

The general case $\beta > 0$. In this case stress is no longer constant in the bar, and the strain in equilibrium configurations is nonuniform in each phase interval. In case of trilinear material (7), the equilibrium equation

$$(\sigma(u_x))_x - 2\beta u = 0 \quad (15)$$

is linear in each phase interval, and the problem of finding elastic equilibria reduces to solving a linear algebraic system [31]. Elastic minimizers for this case are shown in Figure 5(a). Observe that the bounding loop is now tilted. Phase minimizers shown in Figure 5(b) were calculated in [31]. They minimize the potential energy with respect to smooth variations in both elastic field and the positions of the phase boundaries c_i . However, one can show [4] that these equilibria are unstable with respect to the variations introducing new phase boundaries and hence are not strong minimizers of (2). There is an interval of the end displacements I_β where for a fixed $d \in I_\beta$ and a given phase equilibrium with N boundaries, there is always a phase equilibrium, with a larger number of interfaces, that has lower potential energy. For the trilinear material, the interval is given by $I_\beta = [-D_\beta, D_\beta]$, with

$$D_\beta = \frac{e^{\sqrt{\beta}} - 1}{\sqrt{\beta}e^{\sqrt{\beta}/2}}. \quad (16)$$

The difference in energy between a given phase equilibrium and its competitors with lower energy is the largest at $d = 0$ and decreases as d approaches the boundaries of I_β . See Figure 5(c). This is different from the case $\beta = 0$ where any arrangement of phases and any number of interfaces in a phase equilibrium gives minimal (zero) energy. Observe that for positive β one has $D_\beta > 1$ in (16), and hence the interval of metastability (with respect to variations not increasing N) of phase equilibria is larger than the global minimizer interval $[-1, 1]$ in the no-foundation case.

Energy branch of phase equilibria for a given N is the lower envelope of the branches of elastic equilibria with the same N and fixed locations of interfaces. This is shown for $N = 2$ in Figure 5(c).

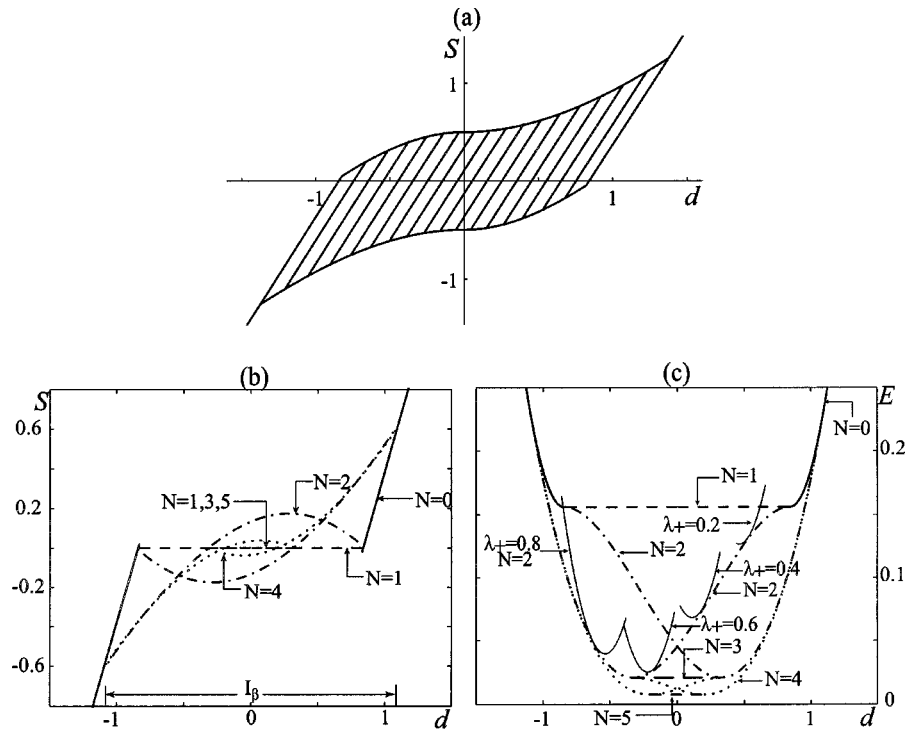


Figure 5. Stable equilibria for the trilinear material (7) with $\tau = 0.75$ in the presence of elastic foundation: $\beta = 2.3$. (a) Load-displacement diagram of stable elastic equilibria. Every point inside and on the loop is an elastic equilibrium. Tilted parallel lines show branches of equilibria with fixed locations of phase boundaries. (b) Load-displacement diagram of phase minimizers. Each curve is a branch of equilibria with different number of interfaces. From [31]. (c) Energy of phase minimizers (thick curves) and several branches of elastic equilibria (thin solid curves) with two interfaces and different volume fractions λ_+ of the + phase.

The elastic equilibria satisfying (12) are even *weaker* energy minimizers than the phase equilibria because variations of c_i are not allowed. However, it has been shown in [32] that dynamic solutions of (3) for the case $\beta = 0$ get stuck in the *elastic* equilibria which are dynamically stable when (12) is satisfied [20]. This causes an interesting stick-slip motion of phase boundaries (see Section 4). We will shortly see that this is also the case when β is nonzero and point out the new effects caused by the presence of the elastic foundation.

4. Dynamics: Main Numerical Results

The initial-boundary value problem (3) with cyclic loading (4) was solved numerically. The finite-difference scheme developed in [26] was adopted, with minor changes required to incorporate time-dependent boundary conditions. The mesh sizes in space and time for a typical computation were chosen to be $\Delta x = 0.005$

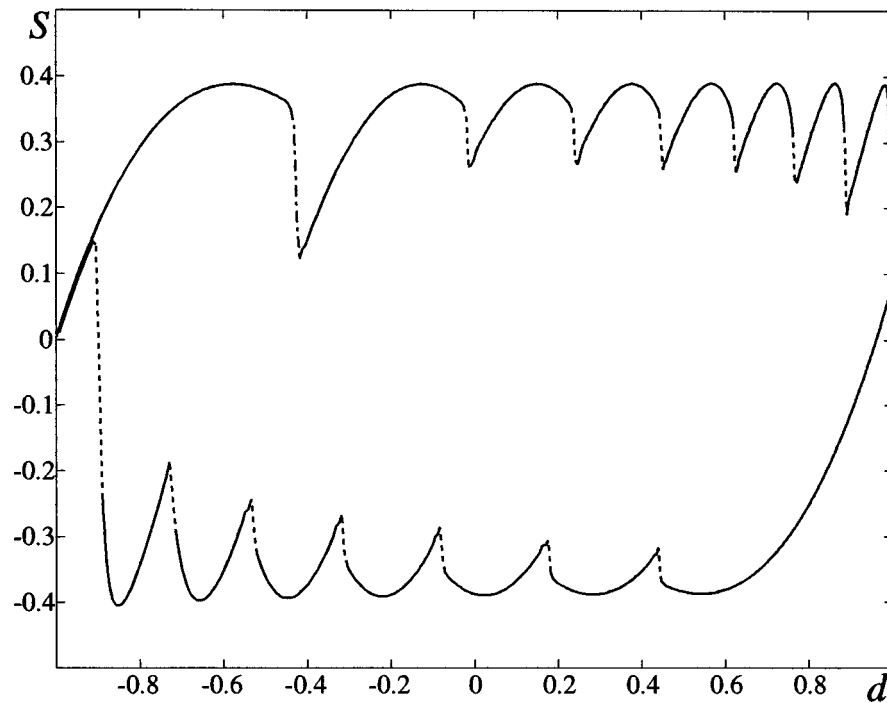


Figure 6. End load S versus d during a loading–unloading cycle from a numerical solution of problem (3) without an elastic foundation: $\beta = 0$, $\gamma = 0.1$, $\rho = 0.05$, $t_T = 100$. Solid, dash-dotted and dashed curves indicate stick, nucleation and slip regimes, respectively. The asymmetry of the loop with respect to the reversal of the loading–unloading path is caused by asymmetric loading rate $d'(t)$ (see Figure 2(b)). From [32].

and $\Delta t = 0.0005$, respectively. Convergence of the numerical method was checked by reducing the mesh sizes in both space and time.

Case $\beta = 0$. This case was studied in [32]. Here we summarize the results. A typical hysteresis loop is shown in Figure 6 where the end load S is plotted against the end displacement d . The most striking feature of the loop is that it possesses a number of serrations, or “teeth”, which are sometimes observed experimentally [9, 19]. Initially, the dynamic solution is close to an equilibrium solution branch with the whole bar in the $+$ phase. Upon reaching the maximum of the first “tooth”, the strain enters the spinodal region where the static solution is unstable. As a result, the strain gradient increases and phase boundaries start to form. Eventually, two sharp phase boundaries form in the middle of the bar. The formation of the boundaries is accompanied by a drop in end load (dash-dotted curve). Now the bar is occupied by the $-$ phase in the middle and the $+$ phases at the ends: $(+, -, +)$. Across each phase boundary, the strain is close to discontinuous. As the loading is continued, the newly formed boundaries do not move but the strain in the regions separated by the interfaces grows. This is called a *stick* regime. It corresponds to a

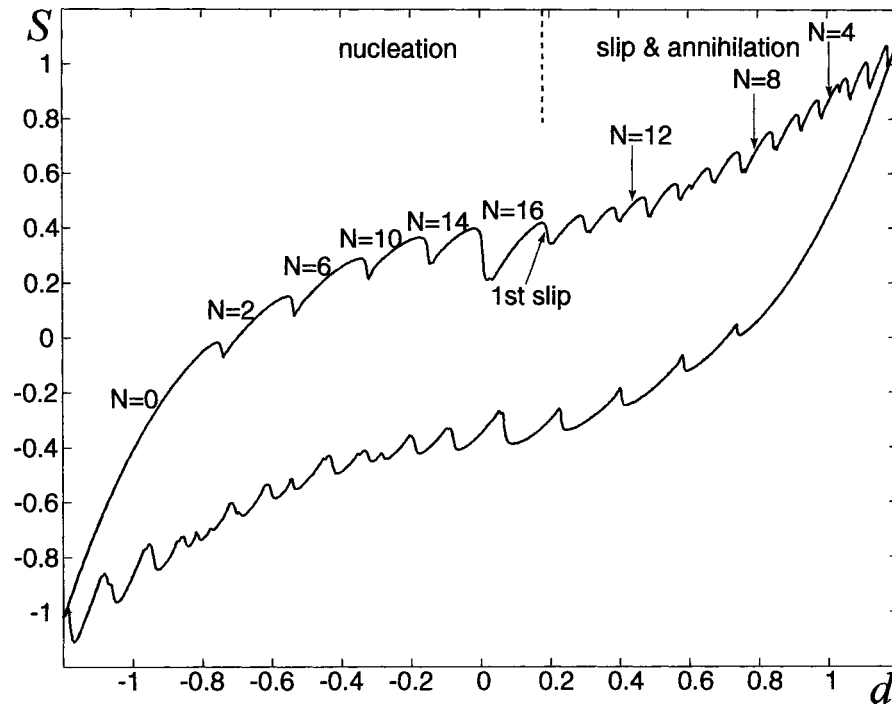


Figure 7. End load S versus d during a loading-unloading cycle from a numerical solution of problem (3) with the elastic foundation present: $\beta = 2.5$, $\gamma = 0.1$, $\rho = 0.05$, $t_T = 100$.

portion of the second tooth where stress grows (solid curve). Eventually, the strains at the ends of the bar enter the spinodal region, and instability again increases the strain gradient until the strain profile smoothens. The old discontinuities are now destroyed and the new ones are formed closer to the ends of the bar. This is called a *slip* regime (dashed curve) and during this regime the stress drops. This process of alternating stick and slip regimes happens several times until the whole bar is in the $-$ phase. It has been shown in [32] that during a stick regime dynamic solution is close to a branch of elastic equilibria with fixed positions of the interfaces. During the slip regime (or nucleation), the system, driven by spinodal instability, jumps from one elastic equilibrium to another. While the number of boundaries is two in this example, more boundaries are formed when $\gamma/\sqrt{\rho}$ is smaller.

Case $\beta > 0$. Let us now consider a case when β is nonzero but the loading and all other parameters are the same as in Figure 6. A typical loop for a sufficiently large β is shown in Figure 7. One apparent difference from Figure 6 is that the hysteresis loop now has a positive slope due to the elastic foundation. The tilted hysteresis loops are sometimes observed in experiments [9, 19]. This feature is perhaps expected because an elastic foundation makes the system stiffer. A more interesting difference from the no-foundation case is that while the “teeth” look much like in the $\beta = 0$ case (although there are many more of them), a large

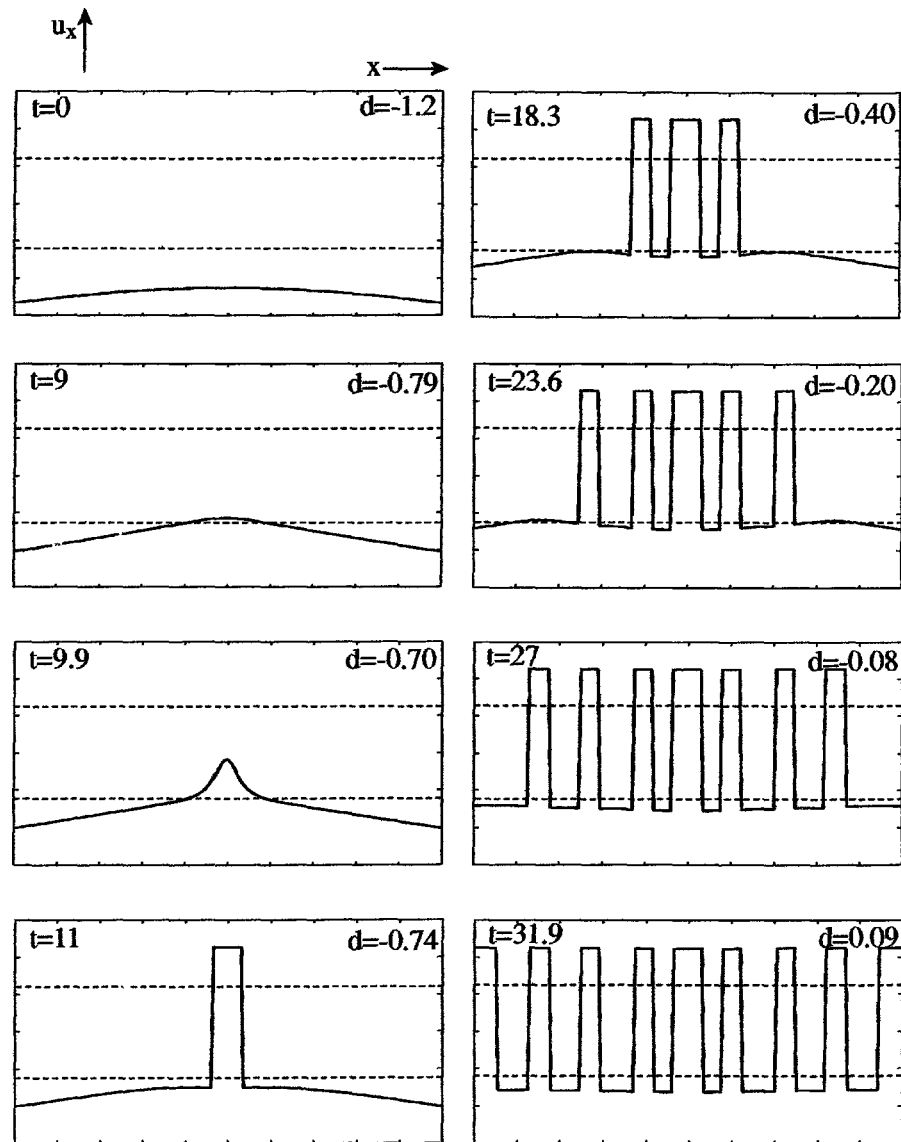


Figure 8. Strain profiles of solutions of (3): nucleation.

number of serrations in this case correspond to the *nucleation* events, and not the stick-slip interface motion. In fact, as long as the end displacement d is nonpositive during loading, *each* serration corresponds to a nucleation of a number of $-$ phase intervals, and only when d is positive, the stick-slip motion of phase boundaries takes place. Recall that in our model the foundation is relaxed at $u' = d_* = 0$. In contrast, in the no-foundation case, only the first stress drop (or a first few ones when $\gamma/\sqrt{\rho}$ is lower, and more boundaries form) is caused by nucleation and the

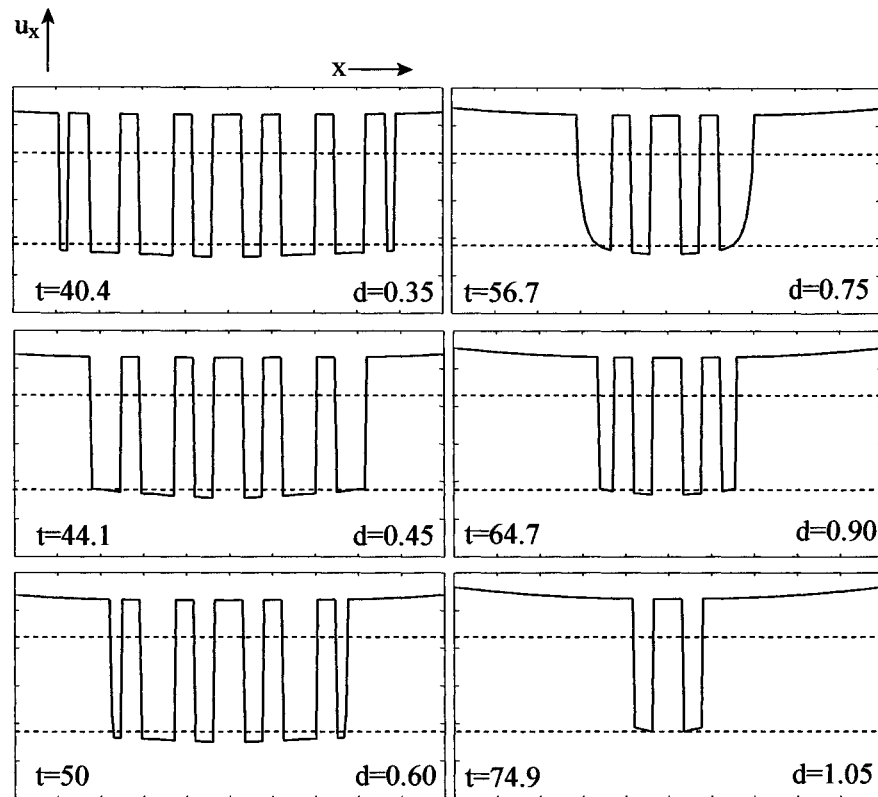


Figure 9. Strain profiles of solutions of (3): interface slip and phase annihilation.

rest correspond to the slip of the interfaces, as described in [32] and above. As a result, more boundaries are formed when $\beta \neq 0$ (sixteen in this case versus only two when $\beta = 0$) via a step-by-step nucleation process, and later these boundaries move towards each other via a stick-slip interface motion.

When two phase boundaries are sufficiently close to each other, they coalesce, and *phase annihilation* takes place. This process, while not seen in Figure 6, where only two boundaries form, occurs in the no-foundation case as well when the number of interfaces is higher (see Figure 13(a) for an example).

Figures 8 and 9 show the change in strain profile as the bar is loaded at different time snapshots. Notice how the mechanism of phase transition changes from — phase nucleation at nonpositive d in Figure 8 to the interface motion and phase annihilation starting with some positive d (see Figure 9). Observe also that nucleation occurs only *in the interior* of the bar until the end displacement becomes nonnegative.

As in the no-foundation case, during a stick regime (the portions of serrations with increasing end load) the solution is close to the elastic minimizers with “frozen” phase boundaries (the number or location of interfaces changes from one

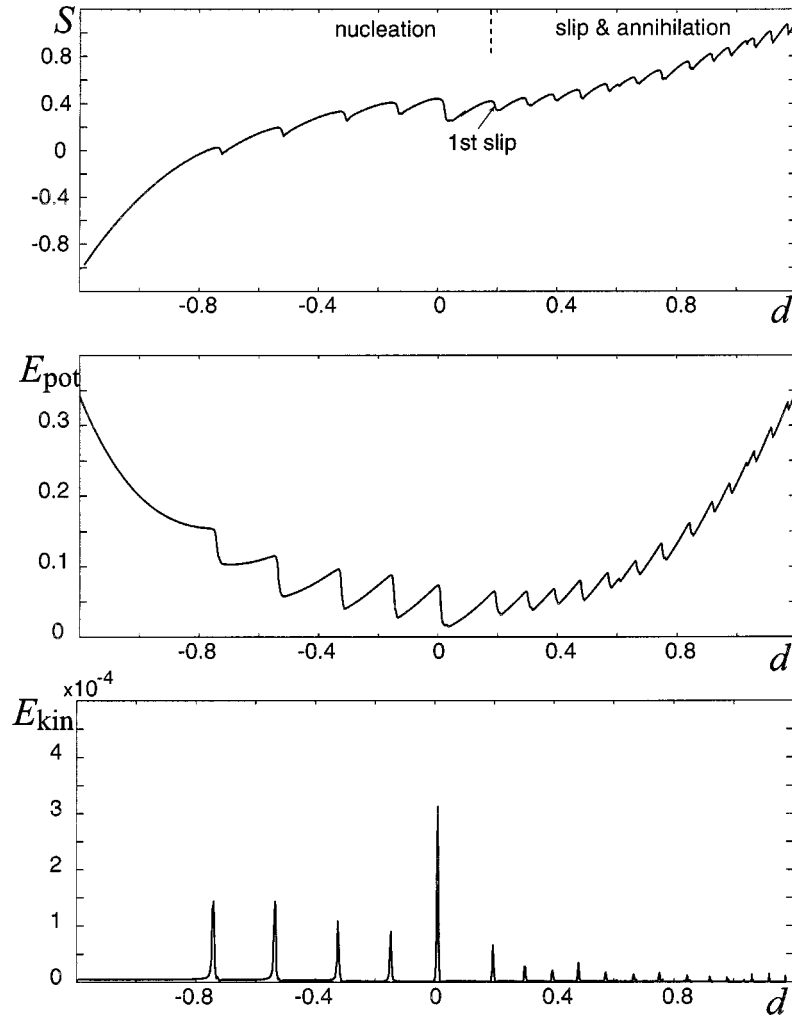


Figure 10. End load, potential energy and kinetic energy during loading: $\beta = 2.5$, $\gamma = 0.1$, $\rho = 0.05$, $t_T = 100$.

tooth to another); these are weak local energy minimizers in the sense explained above. Recall that the total energy rate is given by (5). In a stick regime, the loading power is higher than the dissipation rate, and while kinetic energy is very low, the potential energy grows when loading power is positive (Figure 10). During a slip regime or a nucleation event, the spinodal instability results in rapid growth of the strain gradient. Hence, both kinetic energy and the dissipation rate grow. Eventually, the dissipation rate exceeds the loading power causing the total energy drop. Meanwhile, the system has jumped to another branch of elastic minimizers with either more phase boundaries (nucleation) or some of the existing interfaces moved to the new positions (slip) or destroyed (annihilation).

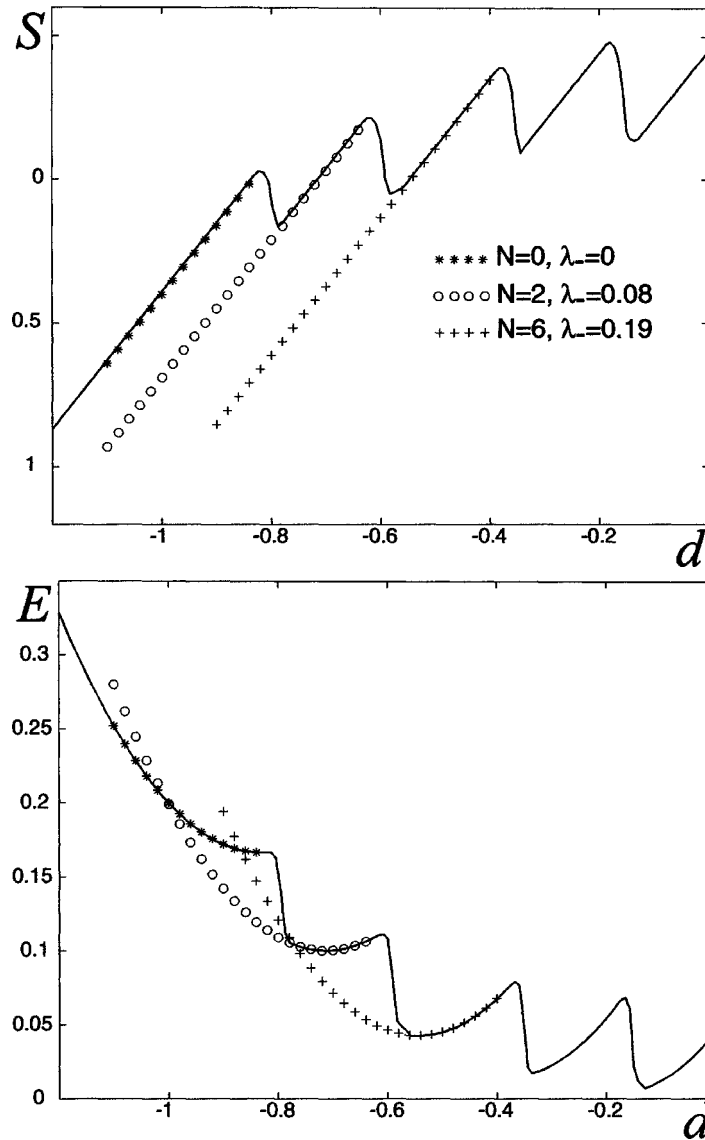


Figure 11. Comparison of end load $S(d)$ and energy $E(d)$ of the dynamic solution of problem (3) for a trilinear material (7), $\tau = 0.75$ (solid line), to the quasistatic branches of elastic minimizers with fixed positions of phase boundaries: $\beta = 2.5$, $\gamma = 0.1$, $\rho = 0.05$, $t_T = 100$. The locations of the boundaries are chosen from the dynamic solution. N is the number of boundaries and λ_- is the volume fraction of the $-$ phase.

While analytical calculation of elastic equilibria for the fully nonlinear energy density (1) and nonzero β is difficult due to the nonlinearities involved, it reduces to solving a linear system of algebraic equations in case of a trilinear material (7). Figure 11 compares the S - d diagram for the dynamic solution to a few quasistatic branches of elastic minimizers with fixed locations of phase boundaries. Positions of the interfaces on the quasistatic branches are taken to be the same as in the dynamic solution. Like in [32], the dynamic solution jumps from one quasistatic branch to another.

Figure 12 shows some details of the three phase transformation processes observed: phase nucleation, interface slip and phase annihilation. In all three regimes, the solution is initially close to one of the elastic minimizers (strain profiles at times a , g , n in Figures 12(c)–(e)). Due to the elastic foundation, the strain is nonuniform in each phase interval. Continued loading results in increasing strain in each interval. Eventually strain in a portion of a former $+$ interval (during loading) enters the spinodal region. Thereupon the strain gradient rapidly grows due to instability. This results in pushing a portion of the bar into the $-$ phase. The solution then approaches another elastic minimizer. During nucleation of a new $-$ interval (Figure 12(c)), the strain profile sharpens, forming two new interfaces. During the interface slip event (Figure 12(d)), the strain profile smoothens, destroying an old interface and then sharpens, forming a new one at a different location. During annihilation (Figure 12(e)), an entire interval that was formerly in the $+$ phase enters the $-$ phase, and a pair of interfaces is destroyed.

Observe that all three phase transformation processes occur via spinodal decomposition, happening inside (nucleation), on a boundary of (slip) a single phase domain and covering a whole domain (annihilation). Each process happens after a portion of the bar has strain in the spinodal region, and there is no energy barrier crossing. However, in terms of interface dynamics, these are very different processes, involving formation, motion and coalescence of phase boundaries. It is therefore important to understand under what conditions each process is preferred in the model.

The absence of the slip events at negative d is observed at large enough β for a given loading, or at slow enough loading at a given β . The critical foundation stiffness β_{cr} marking the onset of this behavior depends on the loading acceleration (controlled by the parameter t_{T} in (4)) and the density ρ in the reference configuration. The slower the loading or the smaller the density, the less β_{cr} . With the loading and inertia parameters chosen in the examples above ($t_{\text{T}} = 100$, $\rho = 0.05$), no slip occurs at negative d for $\beta > 10^{-6}$. As β is decreased, the largest number of interfaces, and therefore the number of nucleation events, decrease, and the slope of the hysteresis loop becomes smaller. At small β ($\beta < 10^{-6}$), slip is observed at negative d , and the solution approaches the $\beta = 0$ case.

The transition from slip-dominated solution behavior observed at small β to the dynamics with no slip events at negative d as in Figure 7 is seen clearer at higher values of density ρ . For example, in Figure 13 ($\rho = 1$ instead of $\rho = 0.05$; γ and

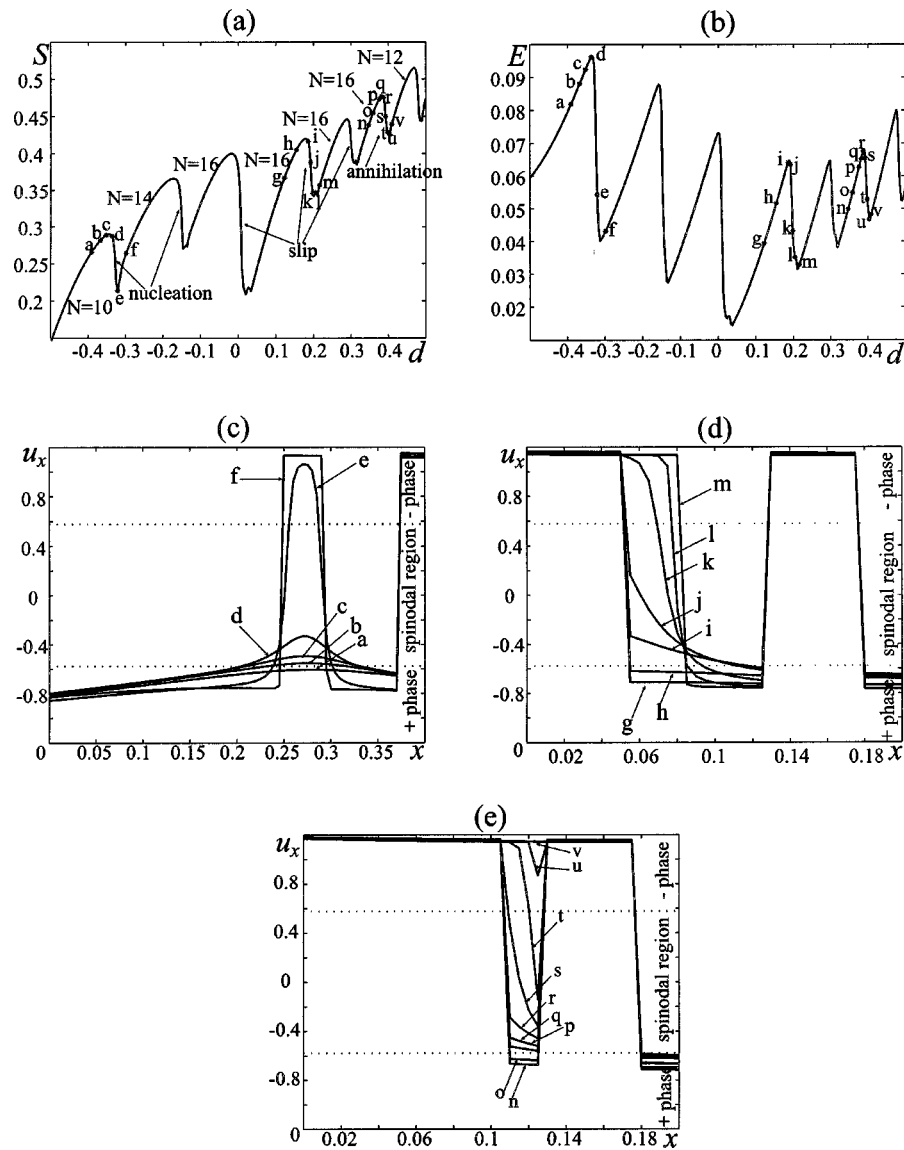


Figure 12. Typical nucleation, slip and annihilation processes observed in Figure 7 during loading: (a) end load and (b) potential energy diagrams and strain profiles during (c) nucleation, (d) slip and (e) annihilation. The letters a–v indicate different time snapshots. The mesh size in space is $\Delta x = 0.005$.

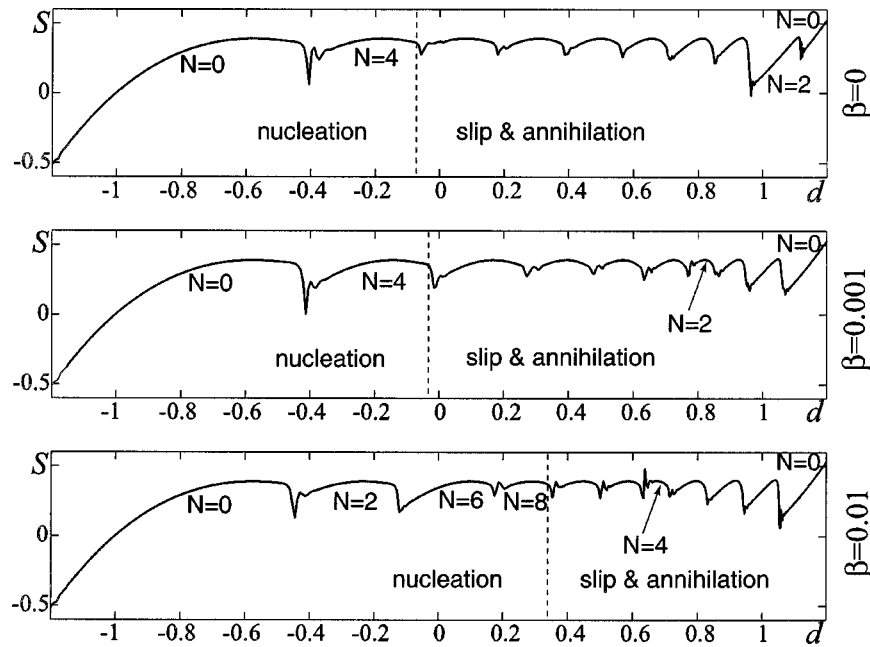


Figure 13. The transition from slip-dominated solution behavior at $\beta < \beta_{cr}$ ($\beta = 0, 0.001$) to the dynamics with the first slip event at positive d ($\beta = 0.01 > \beta_{cr}$). The parameters are $\rho = 1$, $\gamma = 0.1$, $t_T = 100$. If the number of boundaries is not written next to a tooth, it is the same as on the previous one. Such a tooth follows a slip event. The dashed vertical lines mark the start of the first slip event in each case. The end-load oscillations, not seen in the previous examples, during nucleation, slip and annihilation events, are due to the lower effective viscosity $\gamma/\sqrt{\rho}$ in this case (see also Section 7).

t_T are the same as in Figure 7) we show the end load $S - d$ diagrams at different values of β . At $\beta = 0$ and $\beta = 0.001$ after formation of four boundaries during a nucleation event, the dynamics is dominated by slip and annihilation events, with the first slip (marked by a dashed vertical line) occurring at $d < 0$. At $\beta = 0.01$, however, the dynamics is similar to that exhibited in Figure 7: step-by-step nucleation of up to eight boundaries is followed by slip and annihilation events. In this case the first slip occurs at positive d . See Figure 13.

So why does slip not occur at $d < 0$ and $\beta > \beta_{cr}$ and become possible only when d is positive? And what causes the transition in solution behavior? To answer these questions, we will need to examine how the strain profiles in elastic equilibria change with the loading.

5. The Elastic Minimizers

While the analytical calculation of equilibria can be difficult or even impossible depending on the energy density chosen, some important information may be obtained from the phase plane analysis. For the sake of explaining some of the

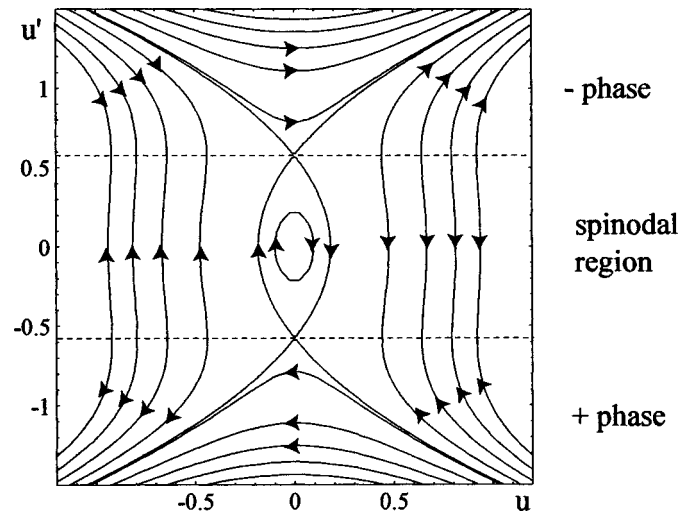


Figure 14. Phase plane of equilibrium solutions of problem (3).

numerical observations discussed above, we will concentrate on the case of energy density (1) noting that the results can be easily generalized to any double-well potential provided the elastic foundation is relaxed at strain corresponding to the maximum of the spinodal region. And while we study the symmetric boundary conditions case

$$u(0) = -\frac{d}{2}, \quad u(1) = \frac{d}{2} \quad (17)$$

here, the nonsymmetric boundary conditions case (with one end fixed) is treated similarly. Since the dynamic solutions of (3) are symmetric due to the symmetry in both the boundary and initial conditions and solution uniqueness (shown similarly to the proofs in [4, 32]), we concentrate on *symmetric* equilibria only.

Since equation (3)₁ in the statics case has a first integral (8), one can do a phase plane analysis of equilibria [4]. The phase plane is shown in Figure 14. Observe that there are five kinds of orbits possible: the orbits crossing $u = 0$, with strains in \pm phases; the side orbits, with strains in \pm phases, ending at the boundary of the spinodal region and not crossing $u = 0$; the side orbits, with strains within the spinodal region, crossing $u' = 0$ and located to the right and to the left from the center; the elliptical orbits centered at the origin $(u, u') = (0, 0)$; and a pair of separatrix orbits that separate the elliptic orbits from the rest. The orbits located inside the spinodal region contain the statically unstable equilibria (any solution with strain in the spinodal region is unstable by Legendre's necessary condition). Of interest here is the group of upper and lower orbits that correspond to the $-$ and $+$ phases, respectively. In what follows, we will refer to them as $-$ and $+$ orbits.

Consider an equilibrium having strain entirely in the $+$ phase when $d < 0$. This solution follows one of the $+$ orbits that cross $u = 0$, starting at $u(0) = -d/2 > 0$

and ending at $u(1) = d/2 < 0$. Thus the strain profile reaches its maximum in the middle of the bar. The orbit followed is determined by the condition

$$1 = \int_0^1 dx = \int_{-d/2}^{d/2} \frac{du}{u'} = \int_{-d/2}^{d/2} \frac{du}{g(C - \beta u^2)}, \quad (18)$$

where $g(\xi)$ is the inverse of the function $\phi(u') = W(u') - u'W'(u')$ (one can show that $\phi(u')$ is invertible in the phase intervals) and C is the constant from (8) corresponding to the orbit. Thus, if d is given, one can always solve for C using (18). As we increase d , the strain in the bar grows and the solution follows higher and higher $+$ orbits until it reaches a separatrix orbit and the maximum strain is at the lower boundary of the spinodal region, $u'_{\max} = -1/\sqrt{3}$. One can show that in the case of energy density (1) $C = C_0 = 1/3$ on the two separatrix orbits. In fact, in this case they are given by parabolae

$$u = \pm \frac{3(u')^2 - 1}{\sqrt{12\beta}} \quad (19)$$

in the phase plane. One can calculate the critical value of d when the $+$ phase solution is on a separatrix orbit:

$$d_{\text{crit}} = \frac{2}{\sqrt{12\beta}} \left(1 - \left(\frac{\sqrt{12\beta}}{4\sqrt{3}} + 1 \right)^2 \right) \quad (20)$$

and the value $d_{\text{crit}} = -0.806$ for $\beta = 2.5$ is consistent with the numerical results. At d above d_{crit} there exist no stable single-phase solutions in the $+$ phase.

Once the dynamic solution following this quasistatic branch reaches $d = d_{\text{crit}}$, continued loading results in pushing the middle of the bar into the spinodal region in order to satisfy the boundary conditions. Spinodal instability then forces the system to seek another elastic minimizer with a $-$ phase interval in the middle of the bar.

The fact that the strain profile is *nonuniform* inside the $+$ phase intervals turns out to be crucial in the nonzero β case. Indeed, as the strain in the bar grows due to loading, it is a neighborhood of the maximum strain which is pushed into the spinodal region first and later becomes part of the $-$ phase. Thus we know that when β is sufficiently large, first nucleation will occur *in the middle of the bar* because this is where the strain is maximal (in case of nonsymmetric boundary conditions with one end fixed, the $-$ phase will nucleate at the fixed end). In contrast, when $\beta = 0$, the first nucleation occurs after the *whole* bar gets into the spinodal region, and the strain-gradient growth due to instability is determined entirely by the inertia force $\rho d''(t)(x - 0.5)$. While this force affects the strain gradient in the nonzero- β case as well, strain-gradient growth due to the foundation term in (3) is much larger for β large enough (or for slow enough loading), as will be shown in the next section. In a sense, the elastic foundation plays a role of an imperfection that determines to some extent the locations of phase nuclei.

When an elastic equilibrium has one or more phase boundaries, the strain jumps from a $+$ to a $-$ orbit (or vice versa) in such a way as to ensure the continuity of both the displacement u (only vertical jumps are allowed in phase plane) and the elastic stress $\sigma(u_x)$ (but the value of stress is allowed to vary from jump to jump). The jumps may occur only within the strain interval in which the equation $\sigma(w) = \text{const}$ has a nonunique solution. In the case of (1) this interval is $[-2/\sqrt{3}, 2/\sqrt{3}]$. The strain profile in each $+$ phase interval has either a *bump* (maximal strain occurs in the interior of the interval, e.g., interval AB in Figure 22 in Appendix) or a *slope* (maximal strain is at either end of the interval, e.g. interval EF in Figure 22). When they get into the spinodal region, the bumps, as we shall see, induce a *phase nucleation in the interior* of the bar. The slopes promote the nucleation of a $-$ phase interval at an end of the former $+$ interval. This involves either a *phase nucleation at an end* of the bar or a *slip of an interface*. To understand which of these mechanisms is preferred when $d < 0$, let us examine the strain profiles of the multiphase elastic equilibria.

In the following, we consider *symmetric* elastic minimizers with two or more interfaces. We make the following **assumptions**:

- (1) $d < 0$;
- (2) a $-$ phase interval is in the middle of the bar;
- (3) $+$ phase intervals are at the ends of the bar.

These assumptions are consistent with the above observation that the first nucleation of $-$ phase occurs in the middle of the bar. With these assumptions, we can prove the following (see Appendix for the proofs):

PROPOSITION 1. *There are at least two $+$ phase intervals with a bump.*

The next proposition ensures that at least one bump reaches the spinodal region first:

PROPOSITION 2. *There exists a $+$ interval with a bump that has higher maximum strain than any $+$ interval with a slope.*

Propositions 1 and 2 together show that when $d < 0$ (with the assumptions made) there exists at least a pair of $+$ intervals with bumps at which the strain is the highest. The neighborhoods of these bumps reach the spinodal region first, promoting $-$ phase nucleation *in the interior* of the bar. That the bumps on the strain profile are the precursors of the future $-$ phase intervals can be seen in Figure 8 when $d < 0$.

Let us now consider the case of $d \geq 0$. In what follows we assume a symmetric elastic minimizer with a $-$ phase interval in the middle. The ends of the bar could be in either $+$ or $-$ phase. We claim that when d is nonnegative and these assumptions hold, an elastic minimizer may have a $+$ interval with a *slope* that has the highest maximum strain among the $+$ intervals.

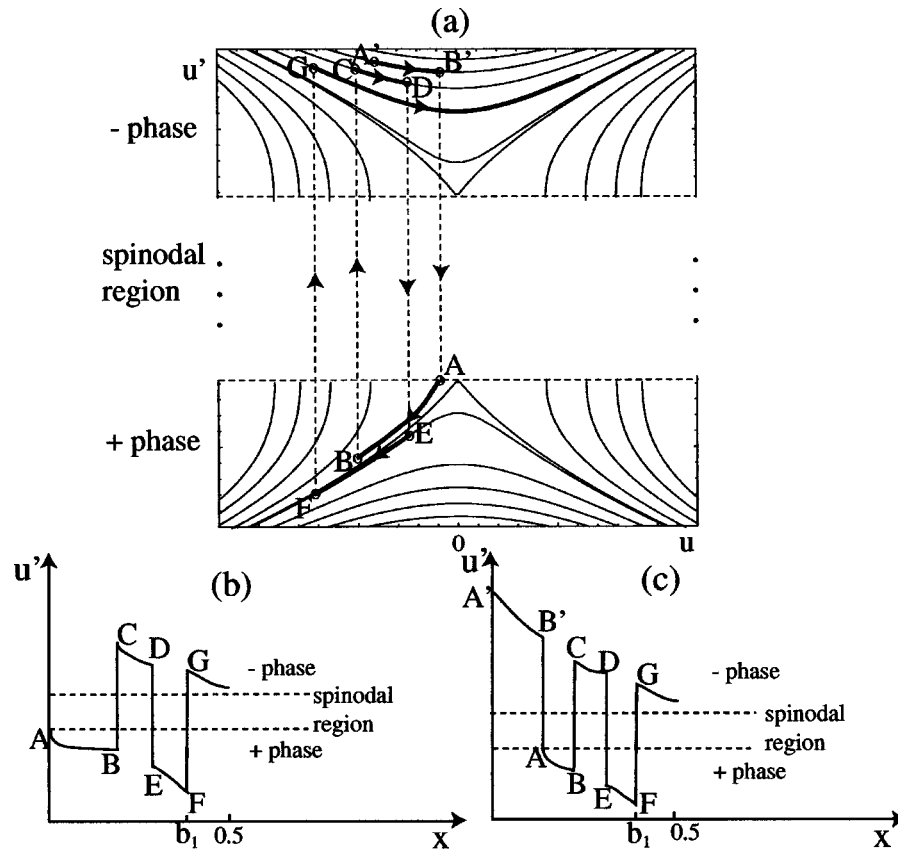


Figure 15. An example of strain profile of an elastic minimizer at $d \geq 0$ (not to scale).

Indeed, suppose that in all $-$ phase intervals except the middle one solution does not cross $u = 0$. This is now possible since at the starting point $x = 0$ we have $u(0) = -d/2 \leq 0$ and one can construct a sequence of $+$ and $-$ phases that reaches the end $u(b_1) < 0$ of the middle $-$ interval $[b_1, b_2]$ without ever crossing $u = 0$ (for $d = 0$ this sequence would have to start with a $+$ phase (downward) interval). Moreover, one expects the solution to cross $u = 0$ only in the middle when d is large enough. According to the phase plane arrows, the above restriction means that in the $+$ intervals the solution also does not cross $u = 0$. Since in both $+$ and $-$ phases the strain (and stress) will decrease in each interval, by the same reasoning as in the proof of Proposition 2 (see Appendix), the solution in the interval $x \in [0, 0.5]$ will climb down the orbits until it reaches $u = 0$ at $x = 0.5$. See Figure 15.

If a $+$ interval is at the ends of the bar when $d \geq 0$, in the example given above these intervals have a downward slope (e.g., interval AB in Figure 15(b)), and the maximum strain in the $+$ phase occurs at the ends. As d grows, these end intervals eventually get onto either a separatrix or a side (not crossing $u = 0$) $+$ orbit, with

the highest strain reaching the spinodal region. In Section 6 we will see that this promotes nucleation of $-$ phase intervals *at the ends of the bar*. This is indeed the case in the numerical simulations (see Figure 8, $d = 0.09$).

Now imagine that there are $-$ intervals at the ends of the bar. In our example this means that the highest strain in the $+$ phase now occurs at the ends of the $+$ intervals that are adjacent to the $-$ intervals at the ends of the bar (intervals AB and $A'B'$, respectively, in Figure 15(c)). As will be shown in Section 6, this promotes a *slip* of an existing interface rather than creation of a new one. In this case the system jumps to another branch of elastic minimizers with the same number of boundaries on which a pair of boundaries have different locations (see Figure 9, $d = 0.45$ and $d = 0.60$ and Figures 12(a), (d)). When a pair of boundaries are close enough after a few slip motions, the two boundaries *coalesce* and the number of interfaces decreases (see Figures 7 and 9).

6. Linearized Dynamics. Discussion

In the previous section we have seen that the elastic minimizers contain $+$ intervals with either a bump or a slope, depending on the sign of d (or, for a more general double-well energy density, whether d is less or greater than the value of strain d_* that gives the maximum energy density and relaxes the elastic foundation). In this section we will explain why, once such a bump or slope enters the spinodal region, the instability will cause the strain gradient to grow in such a way as to promote either a phase nucleation or a slip motion of an interface. In order to do this, we again employ the trilinear material (7) which makes the dynamic equation $(3)_1$ linear in each of the phase or spinodal intervals and therefore allows the use of the Fourier method.

Suppose we have a portion of the bar in the spinodal region. Let this portion have length $l < 1$ (recall that the bar has unit length). Consider the following auxiliary problem:

$$\begin{cases} \rho u_{tt} = [-\theta u_x + \gamma u_{xt}]_x - 2\beta u, \\ u(0, t) = d_0(t), \\ u(l, t) = d_l(t), \\ u(x, 0) = u_0(x), \\ u_t(x, 0) = 0, \end{cases} \tag{21}$$

where $|u_{0x}(x)| \leq \tau$ and τ and θ are the trilinear material parameters from (7). Observe that the linear PDE $(21)_1$ holds for the (nonlinear) trilinear material as long as $u_x(x, t)$ lies within the spinodal region $[-\tau, \tau]$. Assume that $d'_0(0) = d'_l(0) = 0$.

With the change of variables

$$\begin{aligned} v(x, t) &\equiv u(x, t) - (d_l(t) - d_0(t))\frac{x}{l} + d_0(t), \\ v_0(x) &\equiv u_0(x) - (d_l(0) - d_0(0))\frac{x}{l} + d_0(0) \end{aligned} \tag{22}$$

(21) becomes

$$\begin{cases} \rho u_{tt} = [-\theta v_x + \gamma v_{xt}]_x - 2\beta v + \rho f(x, t), \\ v(0, t) = 0, \\ v(l, t) = 0, \\ v(x, 0) = v_0(x), \\ v_t(x, 0) = 0, \end{cases} \quad (23)$$

where

$$f(x, t) = -(d_l''(t) - d_0''(t))\frac{x}{l} - d_0''(t) - 2\frac{\beta}{\rho} \left((d_l(t) - d_0(t))\frac{x}{l} - d_0(t) \right). \quad (24)$$

The solution to (23) can be found as the sum of two terms:

$$v(x, t) = v_h(x, t) + v_i(x, t). \quad (25)$$

The first term, $v_h(x, t)$ solves the homogeneous problem ($f(x, t) = 0$ in (23)) with nonzero initial condition. Using the Fourier method, one finds it to be given by

$$v_h(x, t) = \sum_{n=1}^{\infty} v_h^n(t) \sin \frac{\pi n x}{l} = \sum_{n=1}^{\infty} \frac{v_{0n}}{w_n^1 - w_n^2} (-w_n^2 e^{w_n^1 t} + w_n^1 e^{w_n^2 t}) \sin \frac{\pi n x}{l}. \quad (26)$$

Here v_{0n} are the Fourier coefficients of $v_0(x)$. The exponents $w_n^{1,2}$ in (26) take values

$$w_n^{1,2} = \frac{\gamma k_n^2}{2\rho} \left(-1 \pm \sqrt{1 + \frac{4\theta\rho}{(\gamma k_n)^2} - \frac{8\beta\rho}{(\gamma k_n^2)^2}} \right) \quad (27)$$

when $k_n \equiv \pi n/l > k_{cr}$, where

$$k_{cr} = \sqrt{\frac{\theta}{2\rho} \left(\sqrt{1 + \frac{2\gamma^2\beta}{\rho\theta^2}} - 1 \right)}. \quad (28)$$

Observe that w_n^1 is positive when $k_n > k_0 \equiv \sqrt{2\beta/\theta}$ and negative otherwise, while w_n^2 is always negative. When $k_n < k_{cr}$, $w_n^{1,2}$ are complex with negative real parts.

Figure 16 shows w_n^1 at $k_n > k_{cr}$. Since it is real and positive for $n > n_0 \equiv k_0 l/\pi$, this exponent is responsible for the instability growth. Figure 17 shows the graph of the amplitude $A_n = |v_h^n(t)|$ of the homogeneous term (26) at fixed t and $k_n > k_{cr}$. Observe that a finite interval of modes is amplified the most; the higher is γ , the lower are the modes that are amplified the most. Notice also that the shorter is the portion of the bar that has strain in the spinodal region, the lower are the modes that are amplified the most and the higher is the amplitude. Thus, short spinodal intervals promote a low-mode growth of the homogeneous term.

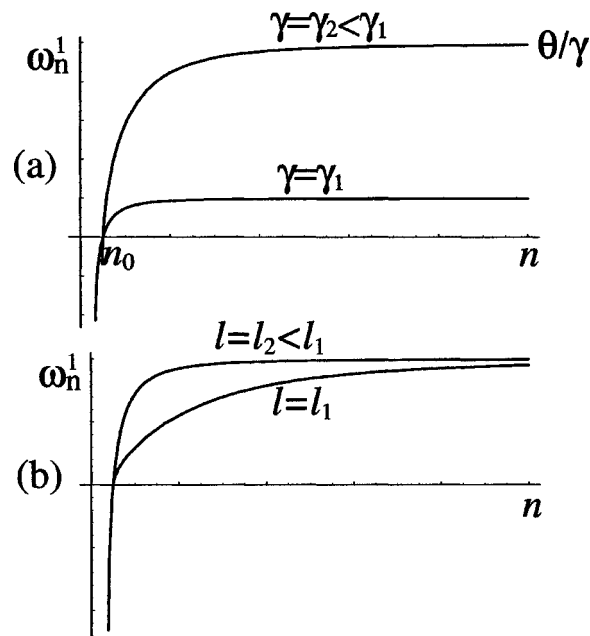


Figure 16. Graph of $w_n^1(n)$ at $k_n > k_{cr}$: (a) at different values of viscosity coefficient γ ; (b) at different values of length l of the interval.

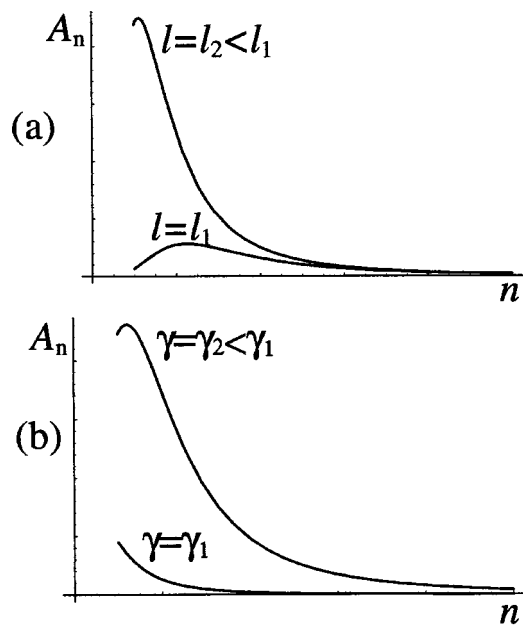


Figure 17. Graph of the amplitude of the homogeneous term (26) $A_n = |v_h^n(t)|$, t fixed, at $k_n > k_{cr}$: (a) at different values of length l of the interval; (b) at different values of viscosity coefficient γ . The initial data is $v_0(x) = (x/l)(1 - 2x/l)(1 - x/l)$.

The second term in (25) solves the inhomogeneous part of (23) with zero initial conditions and is given by

$$v_i(x, t) = \sum_{n=1}^{\infty} v_n^i(t) \sin \frac{\pi n x}{l}, \quad (29)$$

where

$$\begin{aligned} v_n^i(t) &= \frac{2}{\pi n(w_n^2 - w_n^1)} \int_0^t (e^{w_n^2(t-\xi)} - e^{w_n^1(t-\xi)}) g_n(\xi) d\xi \\ &\equiv \int_0^t B_n(t - \xi) g_n(\xi) d\xi. \end{aligned} \quad (30)$$

Here $g_n(t)$ are determined from the boundary conditions and found to be

$$g_n(t) = \begin{cases} -\left(d_l''(t) + d_0''(t) + \frac{2\beta}{\rho}(d_l(t) + d_0(t))\right) & n \text{ odd,} \\ d_l''(t) - d_0''(t) + \frac{2\beta}{\rho}(d_l(t) - d_0(t)) & n \text{ even.} \end{cases} \quad (31)$$

Figure 18 shows the kernel

$$B_n(t) = \frac{2}{\pi n(w_n^2 - w_n^1)} (e^{w_n^2 t} - e^{w_n^1 t}) \quad (32)$$

of the integral in (30) at $k_n > k_{cr}$ and fixed t . The observations made above for the homogeneous term are also true for the nonhomogeneous contribution: shorter spinodal intervals and lower γ promote the low-mode growth.

Now assume that during a very slow loading process a portion of the bar that was previously in the + phase has been pushed into the spinodal region. The length of this portion, l , will change with time, so strictly speaking, the above analysis does not apply even for a trilinear material. Nevertheless, it can give us some idea of how the instability process will evolve locally in space and time.

Suppose that the portion of the bar that has appeared in the spinodal is part of a *bump* in strain profile (as defined in the previous section). Then the initial data, $v_0(x)$, is predominantly low-mode (the Fourier coefficients v_{0n} tend to zero as n goes to infinity). Moreover, the even modes will dominate due to the symmetry of the phase plane with respect to the $u = 0$ axis (which, in its turn, follows from the symmetry of the foundation term, βu^2). Clearly, the homogeneous term given by (26), will amplify a finite range of low modes composing $v_0(x)$ exponentially fast due to the fact that w_n^1 in (27) is positive at $n > n_0$. See Figure 17. This will result in a rapid strain-gradient growth.

Observe that if β is large enough, some of the very low modes will actually decrease in amplitude because for $n < n_0$ both $w_n^{1,2}$ have a negative real part. However, one can estimate that in order for this effect to take place, one should

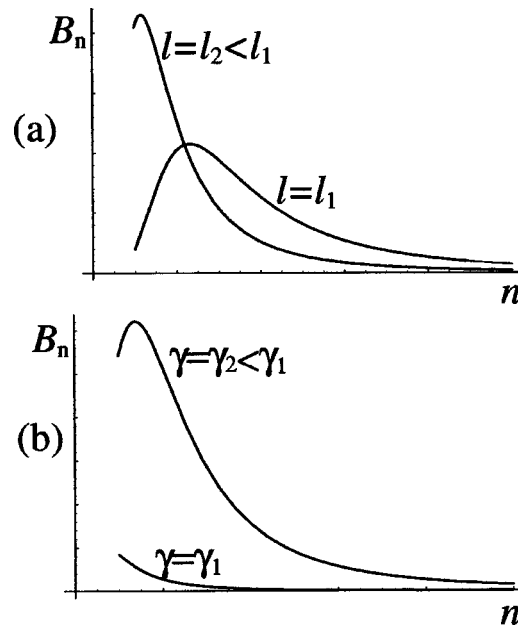


Figure 18. Graph of the kernel (32) of the amplitude of the nonhomogeneous term (29) at fixed t and $k_n > k_{cr}$: (a) at different values of length l of the interval; (b) at different values of viscosity coefficient γ .

have $\beta > 4\pi^2\theta$ which is much greater than the value chosen in the numerical examples described above.

Let us now consider the inhomogeneous term contribution given by (29)–(31). Since we have assumed a slow loading, we can neglect the terms involving the loading acceleration (we can also neglect these terms if we assume a small inertia coefficient). As long as the strain $u_x(x, t)$ in the portion of the bar under consideration is negative, $d_l(t) < d_0(t)$ and $g_n(t) < 0$ for even modes that are predominant in the initial data. At given time instant t , the sign of the convolution integral in (30) is determined primarily by the sign of $g_n(\xi)$ at small ξ since these are multiplied by the largest exponential functions, $e^{w_n^l(t-\xi)}$. Hence, initially the even mode contribution from the inhomogeneous term will grow exponentially in amplitude and have a negative sign. Again, only a finite range of modes will be amplified the most. The smaller is l , the lower is this range. The negative sign of the amplitude $v_n^i(t)$ for even modes implies that strain will be the lowest at the ends of the portion of the bar under consideration. Hence, the strain at the ends of the portion will join the $+$ phase, while the strain in the middle will eventually enter the $-$ phase due to the growing instability. The odd mode contribution will be initially small due to the phase-plane symmetry mentioned above that results in $d_l(0) + d_0(0)$ being close to zero (the odd modes vanish completely during the first nucleation, in the middle of the bar); it will mainly affect the symmetry of the growing bump.

The growing instability causes a highly nonlinear dissipative process (notice that the dissipation rate in (5) has rapidly increased due to the strain-gradient growth) during which the system approaches an elastic minimizer with some amount of $-$ phase *nucleated in the interior*. The strain profile sharpens (see Figure 12(c)) and both end load and potential energy drop (Figures 12(a), (b)).

Now suppose the portion entering the spinodal is a *slope* in the strain profile. Again, one can show that initially $d_l(t) < d_0(t)$ as long as the strain remains negative. One also has that initially $d_l(t)$ and $d_0(t)$ are either both positive or both negative, depending on whether the maximum strain occurs to the left or to the right of the interval with a slope. Clearly, the odd modes are now dominant in both the initial data $v_0(x)$ and the inhomogeneous terms. One shows that the sign of $g_n(\xi)$ at small ξ for odd modes is positive when the maximum strain is at the left end of the portion under consideration and negative otherwise. This means that the odd mode contribution in the inhomogeneous term “cooperates” with the homogeneous mode growth due to the initial data by giving the highest strain at the left (right) end of the portion if it was initially at the left (right) end. The even mode contribution is much smaller due to the same sign of $d_0(t)$ and $d_l(t)$ and affects the convexity of the strain profile in the portion. Hence the end of the portion at which the strain is maximal eventually enters the $-$ phase while the other end is in the $+$ phase. Driven by the instability, the system then approaches an elastic minimizer with increased volume fraction of the $-$ phase. If the original spinodal interval had the highest strain at the end of the bar, *phase nucleation at the end* of the bar takes place. If it was adjacent to a $-$ interval, the former strain discontinuity (at the end where the strain was the highest) is destroyed by smoothening of the strain profile. During a *slip* event, another interface is formed at a different location, so that a pair of interfaces bounding a $+$ interval are now closer. This nonlinear process is described in [32] and shown in Figure 12(d). When two interfaces are close enough, the system prefers to *annihilate* the $+$ interval to adjust the amount of the $-$ phase. See Figure 12(e). In either case, the potential energy drops Figure 12(b)).

Observe that we have not considered the inertial terms involving $d_l''(t)$ and $d_0''(t)$ in (29)–(31) because at slow enough (for a given β) loading (or small inertia coefficient ρ) the contribution of the two other terms caused by the presence of the foundation is much greater. In the no-foundation case these other terms are absent, and the dynamics is determined entirely by the inertial force $\rho[(d_l''(t) - d_0''(t))x/l + d_0''(t)]$. In this case, after a few nucleations, stick-slip interface motion occurs even at negative d [32]. At small enough β for a given loading, the inertia force dominates, and slip becomes possible at negative d . This explains the transition shown in Figure 13.

On the other hand, the inertia term is not as important in (3) when β is nonzero as it is in the no-foundation case. In the latter case, the absence of the inertia force (for example, when the loading function $d(t)$ is linear) results in the non-growth of strain gradient in the spinodal region and the viscous stabilization of the statically unstable states unless there is an initial strain-gradient imperfection. As a result,

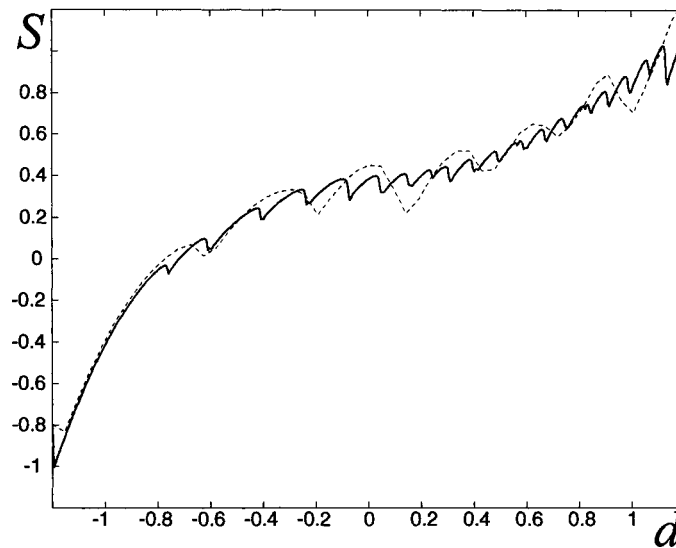


Figure 19. Solution of (3) with the loading rate $d'(t)$ becoming constant after a short initial linear increase from zero: $\beta = 2.5$, $\gamma = 0.1$, $\rho = 0.05$. The solid and dashed curves have the loading rates $d'(t) = 0.02401$ and $d'(t) = 0.2401$, respectively.

numerical simulations in this case are sensitive to any nonuniformities in the strain profile caused by the numerical round-off errors. In the nonzero β case, however, there is always strain-gradient growth within the spinodal region that is caused by the nonuniformity of stress in the elastic equilibria and the foundation term in (3). Figure 19 shows the end load diagram in case of a constant loading rate $d'(t)$.

7. Additional Remarks

In this section, we make some additional observations about the viscoelastic Ericksen's bar on an elastic foundation:

1. As in [32], at smaller loading rates more teeth are observed but they are shallower. See Figures 19 and 20. This happens because at slower loading instability has more time to develop before the system is carried away by the loading, so the jump to another elastic equilibrium branch occurs at smaller d , and hence there are more teeth. In other words, even a little instability creates enough dissipation rate to lower the total energy. On the other hand, kinetic energy is also smaller, and so the system jumps to a closer branch, hence, the shallowness of serrations. During the nucleation stage this means that the intervals of $-$ phase nucleated at every step are smaller, and during the stick-slip stage the boundaries "move" shorter distances. Thus finer and finer phase mixtures form and annihilate as the loading rate decreases. As the loading gets slower, the positive d , at which the number of boundaries is maximal, approaches zero — the value of strain at which

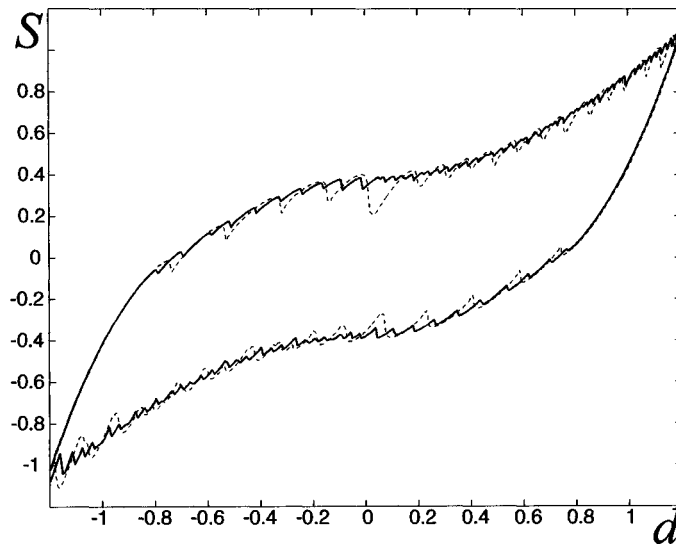


Figure 20. Solution of (3): $\beta = 2.5$, $\gamma = 0.1$, $\rho = 0.05$. Solid curve has slower loading ($t_T = 1000$) than the dashed curve ($t_T = 100$).

the foundation is relaxed (recall that the statics analysis predicts an infinite number of boundaries at zero end displacement). Note, however, that at any small but nonzero loading rate the number of boundaries will be finite and serrations will be present. Unfortunately, at present we do not have an analytical estimate of how the amplitudes of the teeth depend on the loading rate. The numerical results suggest a very slow decrease of the amplitude as we increase t_T , on the order of $1/\ln(t_T)$.

Observe also that as the loading gets slower, the hysteresis loop approaches a certain limiting shape given by the outer envelope of the serrated loops. It is a classical tilted hysteresis loop which is often experimentally observed [9]. Each point on the limiting loop corresponds to either a stable single-phase or a marginally stable multiphase elastic equilibrium. This loop, calculated analytically for a trilinear material (7), is shown in Figure 5(a).

2. More boundaries and teeth also form if the viscosity coefficient γ is lower (with all other parameters kept the same). See Figure 21. This is because, as we have seen in the previous section, at lower γ the instabilities grow much faster, so that the effective loading is slower at lower viscosity. Notice also that at lower γ the end load oscillates in the slip regime before relaxing on an equilibrium branch.

3. The model described in this paper is one of the simple “toy” models designed to gain some intuition about the dynamics of phase boundaries, nucleation and hysteresis. It does not include many aspects affecting the phase transformations such as temperature effects, presence of defects, nonuniformity of the specimen, etc. We emphasize, however, that it does capture many important general features

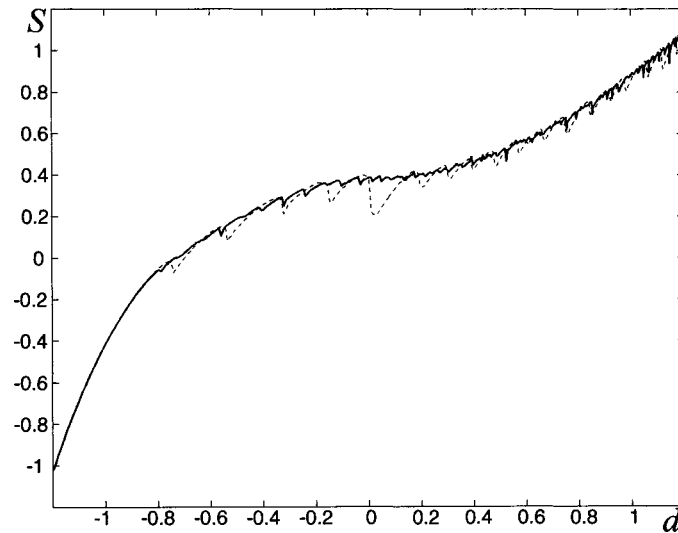


Figure 21. The effect of viscosity coefficient γ on solutions of (3): $\gamma = 2.5$, $t_T = 100$, $\rho = 0.05$. Solid curve has lower viscosity ($\gamma = 0.01$) than the dashed curve ($\gamma = 0.1$).

observed experimentally. A next step is to select more realistic stress-strain laws and choose the foundation coefficient that best matches the resulting loops to the experimentally observed ones. Temperature effects, such as latent heat of the phase transition, are very important [24, 25] and need to be included in the model by selecting a temperature-dependent energy density and accounting for the heat conduction. One can also consider other, more realistic, models of elastic foundation. For example, one can connect the viscoelastic Ericksen's bar to another, linearly elastic bar, via a system of springs. The first bar represents two variants of the martensite phase while the second bar models the austenite phase. The statics of several models of this kind was studied in [30]. The material properties of the second bar may bring some new and interesting effects into the interface dynamics. Such models are currently under investigation.

Acknowledgements

The author would like to thank L. Truskinovsky for very helpful suggestions and comments on an early draft of this paper. The author is also grateful to W. Kalies and P. Swart for kindly allowing to adapt their computer codes for this work.

Appendix

Assume that

- (1) $d < 0$;
- (2) a $-$ phase interval is in the middle of the bar;

(3) + phase intervals are at the ends of the bar.

Proof of Proposition 1. Let $[b_1, b_2]$ denote the boundaries of the $-$ interval in the middle of the bar (in the reference configuration). By symmetry, $b_1 = -b_2 < 0.5$. Symmetry also implies that $u(0.5) = 0$. Since $u'(x) > 0$ in the $-$ phase, we have $u(b_1) < 0$, $u(b_2) = -u(b_1) > 0$. But $u(0) = -d/2 > 0$ by the first assumption. In order to reach $u(b_1) < 0$, the solution has to cross $u = 0$ at least once in the interior of a $+$ phase ($u'(x) < 0$) interval when $x \in [0, 0.5]$. But the point $u = 0$ corresponds to the maximum value of strain on the $+$ orbit. Since this maximum must necessarily occur in the interior of a $+$ interval, there are (by symmetry) at least two $+$ intervals with a bump. \square

Proof of Proposition 2. Assume that an elastic minimizer has several $+$ intervals some of which have bumps and some slopes (if there are only two symmetric $+$ intervals, then by Proposition 1 these intervals contain bumps). Let $x < 0.5$.

1. Suppose a $+$ interval with a bump comes *before* a $+$ interval with a slope. Then two situations are possible:

(a) After a $+$ interval $[c_1, c_2]$ with a bump there is a $-$ interval $[c_2, c_3]$ with a final strain $u'(c_3 - 0) < u'(c_2 + 0)$. Stress is monotonically increasing in the $-$ phase, hence, $\sigma(u'(c_3 - 0)) < \sigma(u'(c_2 + 0))$. By jump condition, $\sigma(u'(c_i - 0)) = \sigma(u'(c_i + 0))$ for any jump point c_i . In the next $+$ interval $[c_3, c_4]$ we will have

$$\sigma(u'(c_3 + 0)) = \sigma(u'(c_3 - 0)) < \sigma(u'(c_2 + 0)) = \sigma(u'(c_2 - 0)), \quad (\text{A.1})$$

i.e., $\sigma(u'(c_3 + 0)) < \sigma(u'(c_2 - 0))$. By monotonicity of stress this implies that $u'(c_3 + 0) < u'(c_2 - 0)$ and, hence, the solution will fall on a $+$ orbit that is *lower* than the $+$ orbit with the bump it was on before. Thus, the maximum strain of the $+$ interval $[c_3, c_4]$ with either downward or upward slope will be lower than the maximum strain of the preceding $+$ interval $[c_1, c_2]$ with a bump (see Figure 22).

(b) Suppose after a $+$ interval $[c_1, c_2]$ with a bump there is a $-$ interval $[c_2, c_3]$ with $u'(c_3 - 0) > u'(c_2 + 0)$. Then, using the same reasoning as above, one can show that the $+$ interval $[c_3, c_4]$ with a slope will be on a higher $+$ orbit than the interval $[c_1, c_2]$ and will have a higher maximum strain (Figure 23). One can construct a whole sequence of such $+$ intervals with an upward slope connected by $-$ intervals with increasing strain. Notice, however, that in this sequence the displacement u must be nonnegative due to the arrows on the phase plane and because the $+$ intervals with a slope cannot cross $u = 0$. But eventually the solution has to cross zero in an interior of a $+$ interval in order to reach $u(b_1) < 0$ where b_1 is the left boundary of the middle $-$ interval as defined in the proof of Proposition 1. Hence, it will have a $+$ interval with a bump on an orbit that is higher than all preceding orbits from the sequence (and higher than the initial $+$ orbit with a bump). This also means that in this case the solution cannot follow the side $+$ orbits with $u > 0$, for otherwise, it is impossible to return to the $u < 0$ side. Thus, in this situation, there is again an interval with a bump that has a higher maximum strain.

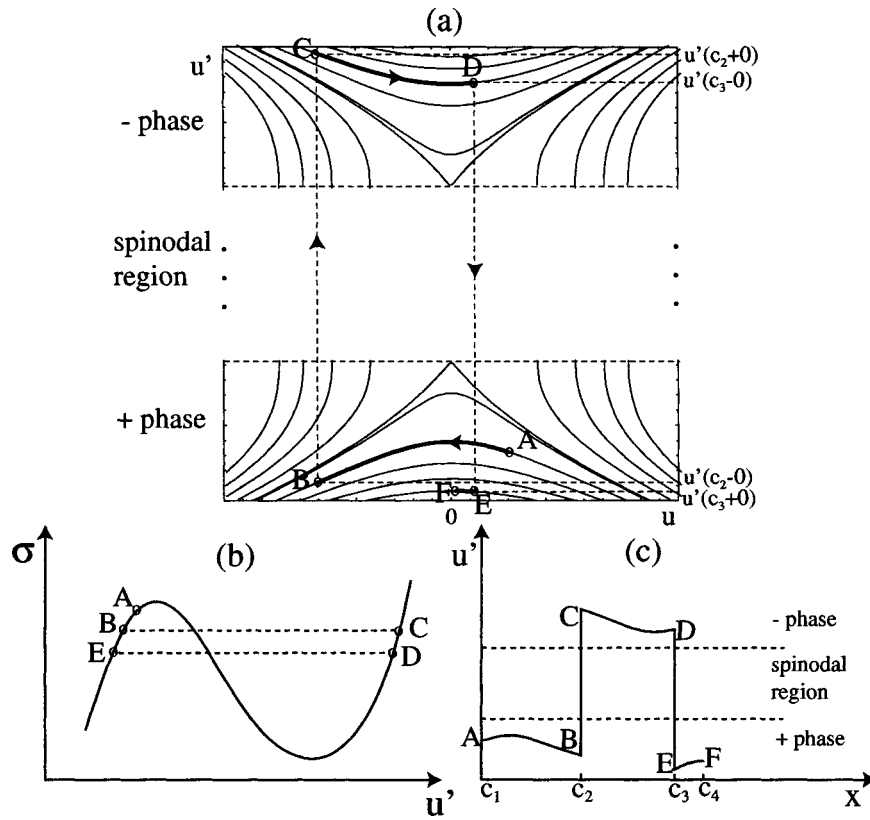


Figure 22. Case 1(a) (not to scale).

If in the $-$ interval $[c_2, c_3]$ the strains are equal at the ends: $u'(c_3 - 0) = u'(c_2 + 0)$, the $+$ interval $[c_3, c_4]$ will be on the same orbit as $[c_1, c_2]$. Since this is an interval with an upward slope, the above argument can be again applied to show that there will be a $+$ interval with a bump on a higher orbit.

Observe that in a special case of a *phase minimizer* the jumps must occur at Maxwell strains $u' = \pm 1$ and, therefore, only intervals with bumps are possible under our assumptions. In this case all of the $+$ intervals will have the same maximal strain.

2. A $+$ interval with a bump comes *after* a $+$ interval with a slope. We again restrict ourselves to $x < 0.5$. There can be two possibilities. The first one is that the initial $+$ interval has a downward slope. Such an interval has nonpositive $u(x)$ and, therefore, must be preceded by a $+$ interval with a bump, due to the boundary condition $u(0) = -d/2 > 0$ and the assumption that we have $+$ intervals at the ends. By reversing the argument in case 1(a) this *preceding* interval with a bump will be on a higher orbit than the one with a downward slope (although the *following* $+$ intervals with a bump may lie on the lower orbits). The second possibility is that the initial $+$ interval has an upward slope. This situation is similar to the case 1(b)

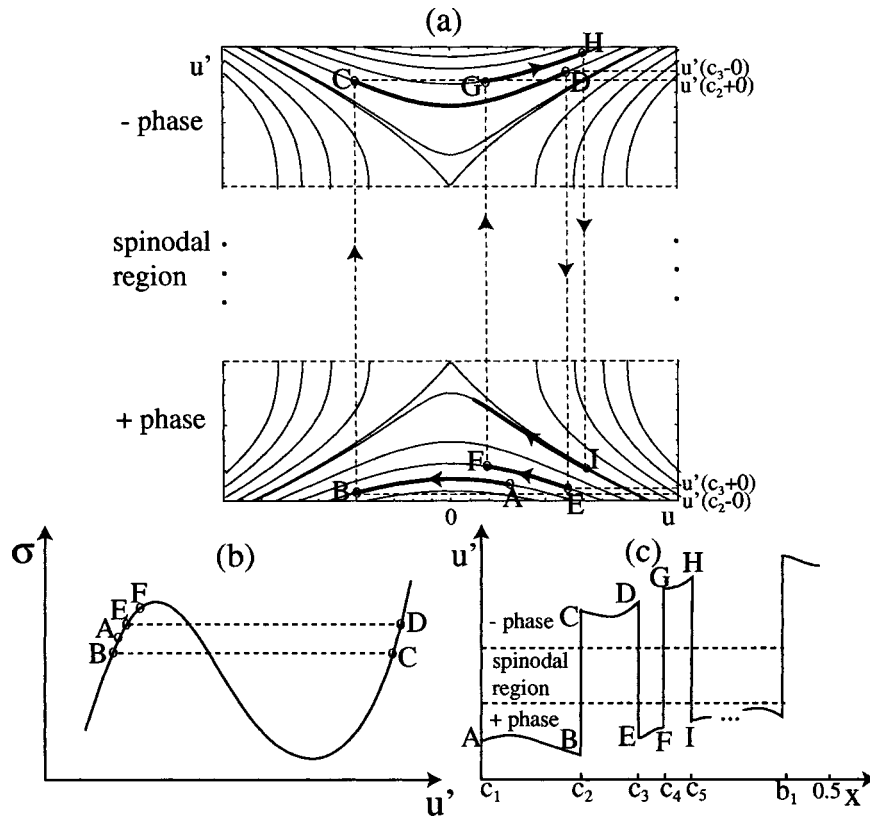


Figure 23. Case 1(b) (not to scale).

after a + interval with an upward slope has appeared: the stress will grow, and the solution will climb up the + orbits but eventually will have to have a + interval with a bump in order to satisfy our assumption of a - phase interval in the middle. That interval will lie on an even higher orbit.

Thus, in either case for any interval with a slope there is an interval with a bump that has a higher maximum strain.

References

1. R. Abeyaratne, C. Chu and R. James, Kinetics and hysteresis in martensitic single crystals. In: *Mechanics of Phase Transformations and Shape Memory Alloys* (1994).
2. R. Abeyaratne and J. Knowles, A continuum model of a thermoelastic solid capable of undergoing phase transitions. *J. Mech. Phys. Solids* **41** (1993) 541-571.
3. J. Ball, C. Chu and R. James, Hysteresis during stress-induced variant rearrangement. *J. Phys.* **5**(8) (1995).
4. J. Ball, P. Holmes, R. James, R. Pego and P. Swart, On the dynamics of fine structure. *J. Nonlinear Sci.* **1** (1991) 17-70.

5. D. Brandon, T. Lin and R. Rogers, Phase transitions and hysteresis in nonlocal and order parameter models. *Meccanica* **30** (1995) 541–565.
6. C. Chu, Hysteresis and microstructures: A study of biaxial loading on compound twins of copper–aluminum–nickel single crystals. PhD Thesis, University of Minnesota (1993).
7. J. Ericksen, Equilibrium of bars. *J. Elasticity* **5** (1975) 191–202.
8. B. Fedelich and G. Zanzotto, Hysteresis in discrete systems of possibly interacting elements with a two well energy. *J. Nonlinear Sci* **2** (1992) 319–342.
9. M. Fremond and S. Miyazaki, *Shape Memory Alloys*, CISM Courses and Lectures, Vol. 351. Springer, New York/Wien (1996).
10. G. Friesecke and J. McLeod, Dynamics as a mechanism preventing the formation of finer and finer microstructure. *Arch. Rational Mech. Anal.* **133** (1996) 199–247.
11. G. Friesecke and J. McLeod, Dynamic stability of non-minimizing phase mixtures. *Proc. Roy. Soc. London A* **453** (1997) 2427–2436.
12. S. Fu, I. Müller, and H. Xu, The interior of the pseudoelastic hysteresis. In: C. Liu, H. Kunsmann, K. Otsuka, and M. Wuttig (eds), *Mat. Res. Soc. Symp. Proc.*, Vol. 246 (1992) pp. 39–42.
13. I. Gelfand and S. Fomin, *Calculus of Variations*. Prentice-Hall, Englewood Cliffs, NJ (1963).
14. R. James, Deformation of shape-memory materials. In: C. Liu, H. Kunsmann, K. Otsuka and M. Wuttig (eds), *Mat. Res. Soc. Symp. Proc.*, Vol. 246 (1992) pp. 81–90.
15. D. Kinderlehrer and L. Ma, The hysteretic event in the computation of magnetization and magnetostriction. In: H. Brezis and J.-L. Lions (eds), *Proc. of Nonlinear Differential Equations and Their Applications*. College de France Sem. (1994).
16. R. Krishnan, Stress induced martensitic transformations. *Material Science Forum* **3** (1985) 387–398.
17. R. Krishnan and L. Brown, Pseudo-elasticity and the strain-memory effect in a Ag-45 at.pct. Cd alloy. *Metallurgical Transactions* **4** (1973) 423–429.
18. I. Müller and P. Villaggio, A model for an elastic-plastic body. *Arch. Rational Mech. Anal.* **65** (1977) 25–46.
19. N. Nakanishi, Lattice softening and the origin of SME. In: J. Perkins (ed.), *Shape Memory Effects in Alloys* (1975) pp. 147–175.
20. R. Pego, Phase transitions in one-dimensional nonlinear viscoelasticity: Admissibility and stability. *Arch. Rational Mech. Anal.* **97** (1987) 353–394.
21. X. Ren and L. Truskinovsky, Finite scale microstructures in nonlocal elasticity. *J. Elasticity* **59** (2000) in press.
22. R. Rogers and L. Truskinovsky, Discretization and hysteresis. *Phys. B* **233** (1997) 370–375.
23. P. Rosakis and J. Knowles, Unstable kinetic relations and the dynamics of solid–solid phase transitions. *J. Mech. Phys. Solids* **45** (1998) 2055–2081.
24. J. Shaw and S. Kyriakides, On the thermomechanical behavior of NiTi. *J. Mech. Phys. Solids* **43** (1995) 1243–1281.
25. T.W. Shield, Orientation dependence of the pseudoelastic behavior of single crystals of Cu–Al–Ni in tension. *J. Mech. Phys. Solids* **43**(6) (1995) 869–895.
26. P. Swart, The dynamical creation of microstructure in material phase transitions. PhD Thesis, Cornell University (1991).
27. F. Theil, Young-measure solutions for a viscoelastically damped wave equation with non-monotone stress-strain relation. *Arch. Rational Mech. Anal.* **144** (1998) 47–78.
28. L. Truskinovsky and G. Zanzotto, Ericksen’s bar revisited: Energy wiggles. *J. Mech. Phys. Solids* **44**(8) (1996) 1371–1408.
29. A. Vainchtein, Stick-slip interface motion as a singular limit of the viscosity–capillarity model. *Math. Mech. Solids* (2000) to appear.
30. A. Vainchtein, T. Healey and P. Rosakis, Bifurcation and metastability in a new one-dimensional model for martensitic phase transitions. *Comput. Methods Appl. Mech. Engrg.* **170** (1999) 407–421.

31. A. Vainchtein, T. Healey, P. Rosakis and L. Truskinovsky, The role of the spinodal region in one-dimensional martensitic phase transitions. *Phys. D* **115** (1998) 29–48.
32. A. Vainchtein and P. Rosakis, Hysteresis and stick-slip motion of the interfaces in dynamic models of phase transitions. *J. Nonlinear Sci.* **9**(6) (1999) 697–719.